Charge Carrier Transport in Copper Phthalocyannie Organic Semiconductor

by

TSANG Sai-wing

A Thesis Submitted in Partial Fulfillment

of the Requirement for the Degree of

Master of Philosophy

in

Electronic Engineering

July 2004

Abstract of thesis entitled:

Charge Carrier Transport in Copper Phthalocyannie Organic Semiconductor

Submitted by Mr. TSANG Sai-wing

for the degree of Master of Philosophy in Electronic Engineering

at the Chinese University of Hong Kong in July 2004.

ABSTRACT

Charge transport is perceived as a key to determine the performance of organic semiconductor devices. Understanding of transport properties and influences by trapping and ambient conditions is very important for designing proper molecular configuration and device structure.

In this thesis, a systematic study of hole transport and trap filling effects in copper phthalocyannie (CuPc) thin films sandwiched in between two gold electrodes by electrical measurements is accomplished. A unique characterization technique, admittance spectroscopy, for organic semiconductor is employed to investigate the charge carrier relaxation inside the organic thin films. The current-voltage (*J-V*) characteristics clearly demonstrate that there exist three different regions in Au/CuPc/Au devices, namely, Ohmic, trap filling, and pure space-charge-limited current (SCLC) regions. For the dynamics of hole transport in CuPc, a field-dependent and dispersive mobility is observed by admittance spectroscopy as a function of applied dc voltage. The zero-field mobility and field-dependent coefficient are equal to $\mu_0 = (2 \pm 0.5) \times 10^{-7}$ cm^2/Vs and $\gamma = 0.017 \pm 0.001$ $(V/cm)^{-1/2}$, respectively. They are in good agreement with those measured by dark

injection space-charge-limited transient currents (DI-SCLC). More interestingly, in the high bias region, a large negative capacitance (strong inductive effect) appears at frequency lower than 1 kHz and its magnitude increases with increasing the dc bias. By combining the capacitance-voltage (*C-V*) and *J-V* characteristics of Au/CuPc/Au devices at the bias within the trap filling region, we propose that the slow trap filling process is responsible for the strong inductive effect. Furthermore, significant changes in hole transport behavior are found under different ambient conditions. The hole mobility has a few times increase and become more dispersive while exposed to higher relative humidity levels. This provides strong evidence that water molecules assist the charge carrier hopping in CuPc films.

ABSTRACT (CHINESE)

電荷輸運被認爲是決定有機半導體器件性能的關鍵因素。理解其輸運性質以及陷阱和環境條件的影響，對選擇適當的有機分子和器件結構十分重要。

在本論文中， 我們通過電學特性測量，系統地研究了在 copper phthalocyannie (CuPc)（酞菁銅）薄膜（夾在兩個金電極之間）中的空穴輸運和空穴陷阱填充效應。 我們利用一種用於有機半導體電學表徵的獨特方法－admittance spectroscopy（導納頻譜），來研究有機薄膜中的載流子弛豫現象。 其電流－電壓 (*J-V*) 特性清楚地顯示出在 金/酞菁銅/金 Au/CuPc/Au (MSM) 結構中存在三個不同的區域， 即歐姆特性區、陷阱填充區、和無陷阱空間電荷限制電流區。 在研究酞菁銅薄膜的空穴輸運動力學機制過程中，通過導納頻譜，我們觀察到一與電場強度相關的彌散空穴遷移率，以及與電場強度的指數關係。其零電場遷移率和電場相關係數分別爲 $\mu_0 = (2 \pm 0.5) \times 10^{-7}$ cm^2/Vs 和 $\gamma = 0.017 \pm 0.001$ (V/cm)$^{-1/2}$， 這些數值與由暗注入空間電荷限制瞬態電流獲得的結果達到一致。有趣的是， 在高電場區， 當頻率低於 1 kHz 時，電容－電壓 (C-V) 出現大的負電容效應（強電感效應）， 而且強度隨著偏置電壓增大而增加。 結合 Au/CuPC/Au 器件在陷阱填充區內的電容－電壓 (*C-V*) 譜以及電流－電壓 (*J-V*) 譜， 我們提出負電容效應是由於慢空穴陷阱填充過程所致。 另外， 我們發現在不同的環境條件下， 空穴輸運行爲有很大的變化。 當樣品暴露在高相對濕度環境下，空穴遷移率會成倍的增大，而且空穴傳輸變得更加彌散化。 這有力得證明了水分子會輔助載流子在酞菁銅薄膜中的跳躍傳輸過程。

ACKNOWLEDGEMENTS

I would like to express my sincere gratitude to my supervisor Prof. J. B. Xu for his genuine and patient guidance, invaluable advices and generous encouragement throughout the past two years of study. His enthusiasm and insight on research and board range of interests are clearly demonstrated in different aspects, particularly by investing a lot of efforts to establish international collaborations.

This thesis would not be possibly prepared without the advice and collaboration among many researchers and scientists. During the two-month collaboration in the Polysilicon TFT Group in Cambridge University in 2003, Prof. Piero Migliorato, Dr. F. Yan, and Dr. D. P. Chu showed me their rigorous attitude towards experimental results. Also Dr. F. Yan was very helpful to initiate the experiments. Within our group, I would like thank Prof. Aaron Ho and Prof. S. P. Wong for their enthusiasms and insight in discussing possible mechanisms and theoretical models, and Dr. M. S. Xu for his initiation of the project on negative capacitance in organic devices. Also I am indebt to Dr. W. Y. Cheung, Dr. N. Ke, Mr W. K Chan, for their sincere and valuable technical assistance.

I gratefully acknowledge all my lab-mates for their kind support and discussions, namely, Mr. A. Jin, Mr. H. Wang, Mr. X. Kun, Mr. X. H. Liu, Mr. Y. W. Lai, Mr. C. F. Chow, Mr. K. C. Lo, Mr. W. C. Law, and Mr. S. Y. Wu. Particularly, I thank Mr. A. Jin for instructing and helping me when I started doing the research in organic solids.

At last, but certainly not least, I am very grateful to my parents for their constant support and encouragement.

This work is partially funded by the Research Grants Council of Hong Kong, particularly, via Grant No. CUHK4372/02E.

TABLE OF CONTENTS

Chapter 1

Introduction

The tremendous development of organic materials in the last 50 years had opened a new era for electronics and optoelectronics technologies. In 1987, the observation of efficient electroluminescence in organic semiconductors by Ching Tang and Steven Van Slyke of Eastman Kodak Co.[1] triggered the intensive researches and developments of organic light emitting diodes (OLEDs). A few years later, light emitting diode based on conjugated polymer (PLED) had also been successfully demonstrated [2][3]. The rapid improvement in life time and luminescent efficiency has brought them into the portable flat-panel display market, while the development in larger area application is in progress. The first commercial product, a car stereo display, was introduced by Pioneer in 1999 as shown in Fig. 1.1. In May of 2004, the first large-screen (40-inch) full-color OLED display based on inkjet printing technology was demonstrated by Seiko Epson Co. as shown in Fig. 1.2.

Figure 1.1. A car stereo, the first commercial product based on organic electroluminescent technology [http://www.pioneer.co.jp].

Figure 1.2. The first large-screen (40-inch) full-color OLED display based on inkjet printing technology [http://www.epson.co.jp].

The advantages promised by OLED technology include:

- Thin, light weight, printable displays;
- Low voltage, low power, emissive source;
- Good contrast;
- High resolution (<5 μm pixel size) and fast switching (1-10 μs);
- Broad color gamut;
- Wide viewing angle;
- Low bill of materials.

Given the harsh realities of competition in the flat-panel display market, the last advantage may become the critical one. New analysis from the Frost & Sullivan (www.semiconductors.forst.com), World Emerging LED Markets, reveals that the high-brightness light emitting diodes market generated revenue of $2.6 billion in 2003 and is expected to reach $5.4 billion in 2007. The OLED market generated $200

million in 2003 and is likely to touch $2.4 billion in 2007.

Recently, organic field effect transistors (OFET), solar cells, and memory cells have also been reported with remarkable performance [4-6]. The operation principles among most of the applications involve several physical mechanisms: charge (electron or hole) injection at the metal-organic interfaces, charge transport in the bulk of organic semiconductor, formation and dissociation of excitons by electron-hole combination or by light excitation, and carrier trapping in localized sites. Fig. 1.3 displays the RGB OLEDs fabricated by our fabrication system.

Figure 1.3 (a) Red, **(b)** Green, and **(c)** Blue OLEDs fabricated in our system.

It is widely known that the efficiency of OLEDs and solar cells are mainly determined by the charge injection and transport processes [7-11]. Understanding the mechanisms of these processes is necessary if one intends to improve device performance and explore novel applications.

The motivation of this thesis is to develop a phenomenological understanding of the behavior of carrier transport in organic semiconductors by investigating the properties of carrier mobility and the influence by carrier trapping, which will be fully discussed in Chapters 2-4. Furthermore, in order to determine how carrier transport property is altered in different ambient conditions, a comprehensive study will be

demonstrated in Chapter 5. Owning to its high chemical and thermal stability and wide range of applications, copper phthalocyannine (CuPc), a hole transport organic semiconductor, is chosen for study. The chemical structure of CuPc is shown below in Fig. 1.4.

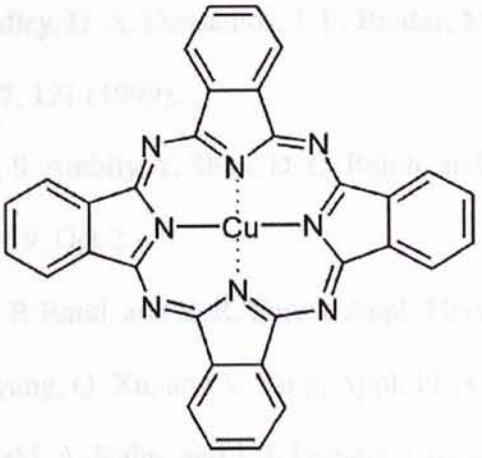

Figure 1.4. The chemical structure of copper phthalocyannine (CuPc).

Reference

[1] C. W. Tang, S. A. Vanslyke, Appl. Phys. Lett. **51**, 913 (1987).

[2] J. H. Burroughes, D. D. C. Bradley, A. R. Brown, R. N. Marks, K. mackay, R. H. Friend, P. L. Burn, and A. B. Holmes, Nature, **347**, 539 (1990).

[3] R. H. Friend, R. W. Gymer, A. B. Holmes, J. H. Burroughes, R. N. Marks, C. Taliani, D. D. C. Bradley, D. A. Dossantos, J. L. Bredas, M. Logdlund, and W. R. Salaneck, Nature, **397**, 121 (1999).

[4] Y. Zhang, J. R. Petta, S. Ambily, Y. Shen, D. C. Ralph, and G. G. Malliaras, Adv. Mater. 2003, 15, No. 19, Oct 2.

[5] J. Xue, S. Uchida, B. P. Rand, and S. R. Forest, Appl. Phys. Lett. 84, 3013 (2004).

[6] L. Ma, S. Pyo, J. Quyang, Q. Xu, and Y. Yang, Appl. Phys. Lett 82, 1419 (2003).

[7] W. R. Salaneck, K. Seki, A. Kahn, and J. J. Pireaux, *Conjugated Polymer and Molecular Interfaces*, Marcel Dekker, Inc., New York (2002).

[8] P. Peumans, A. Yakimov and S. R. Forrest, J. Appl. Phys. **93**, 3693 (2003).

[9] C. D. Dimitrakopoulos and D. J. Mascaro, IBM J. Res. & Dev. **45**, 11 (2001).

[10] P. W. M. Blom and M. C. J. M. Vissenberg, Material Science and Engineering **27**, 53 (2000).

[11] J. N. Bardsley, *IEEE Journal of Selected Topics in Quantum Electronics* **10,** 1 (2004).

Chapter 2

ELECTRONIC STRUCTURE OF ORGANIC SEMICONDUCTOR

Abstract

In this chapter, the molecular structure of organic materials will be discussed. The metal/organic interface is then introduced. It is followed by the discussion of density of state in the bulk and the trap distribution. Experimentally, the surface morphology and crystallinity of CuPc under various substrate temperatures will be introduced. Finally the trap density in Au/CuPc/Au devices will be discussed as well.

2 .1 Introduction of energy profile in organic semiconductors

2.1.1 Organic semiconductors

Organic materials are defined as materials with carbon atoms strongly bonded together. Traditionally, they are believed to be non-conductive and widely used in domestic applications. Owing to the rapid increase of technologies and large efforts from scientists, we now gain more understandings in this class of materials. In 2000, the Nobel Prize for Chemistry was awarded to Alan J. Heeger, Alan G. MacDiarmid and Hideki Shirakawa "for the discovery and development of conductive polymers".

In organic semiconductors the p orbital of carbon in a sp^2-p_z hybrid configuration play a key role. The hybridized sp^2 orbital form σ bonds by covalent interaction which is essential to the molecular structure. The low-energy neutral excitations and charged states are formed from the p_z orbital, which is perpendicular to the plane and overlapping with adjacent carbon atom to form π bond [2][3][4][5]. Fig. 2.1 shows the spatial molecular structure.

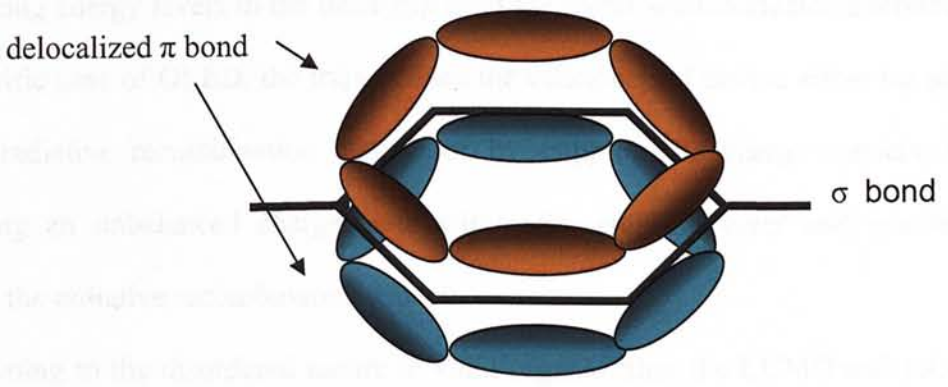

Figure 2.1. Spatial molecular structure or a conjugated molecule.

If more carbon atoms come together, according to the Pauli Exclusion Principle, splitting of the energy level in p_z orbital occurs and eventually forms two energy bands, lowest unoccupied molecular orbital (LUMO) and highest occupied molecular

orbital (HOMO) [6]. However, unlike the continuous conduction and valance bands found in most of inorganic semiconductors, HOMO and LUMO consist of numerous discrete energy levels. In this case, carrsiers have to hopping across the localized site though tunneling process, as shown in Fig. 2.2.

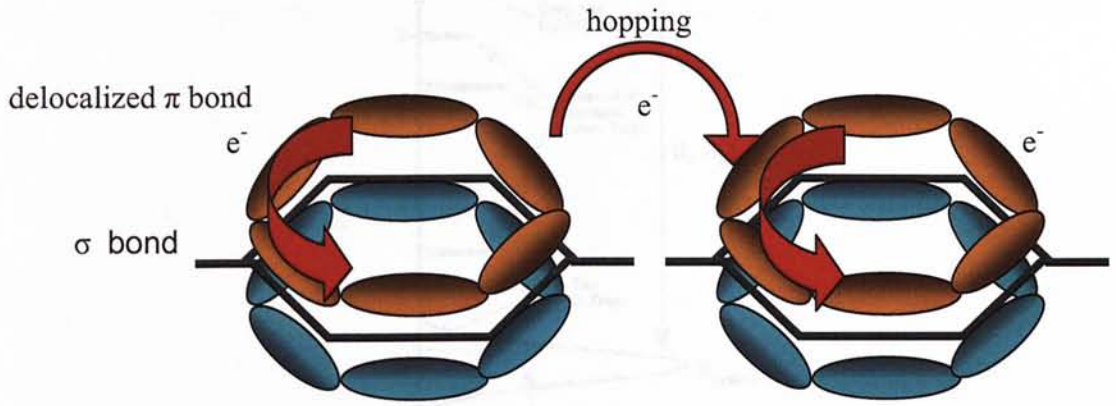

Figure 2.2. Electrons hopping across localized molecular orbital.

2.1.2 Density of state (DOS) and traps distribution

Defect states in semiconductors are known to affect device performance by introducing energy levels in the band gap or at the metal/semiconductor interface. In the specific case of OLED, the traps reduce the efficiency of device either by acting as non-radiative recombination centers or by trapping the charge carriers, thus producing an unbalanced charge state within the emitting layer and eventually limiting the radiative recombination process.

Owning to the disordered nature of solid organic film, the LUMO and HOMO levels form two Gaussian DOS distributions on either side of the carrier energy gap [7][8]. The deep sites in the tails of the two DOS distributions act as continuous, pseudo-exponential distributions of traps in the energy gap [7-10]. The more common sites in the centers of two DOS distributions act as the transport sites between which the carriers hop. Moreover, structural defects or chemical impurities

also induce some discrete single energy traps in the carrier energy gap. The energy diagram in this case is depicted in Fig. 2.4.

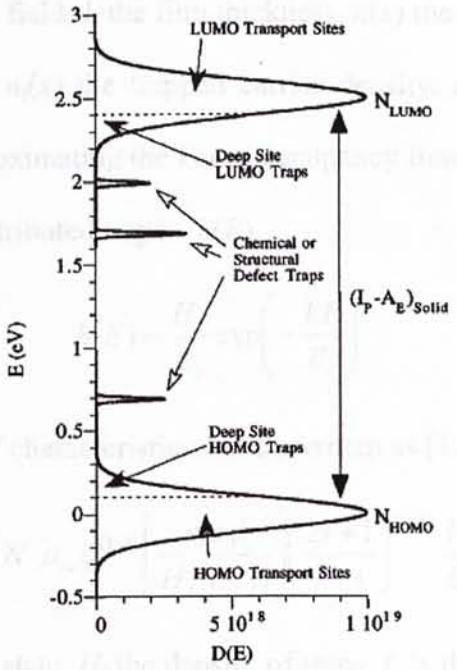

Figure 2.4. A complete picture of the deep site trapping model proposed by A. J. Campbell *et. al* [7] for disordered molecular materials. The LUMO and HOMO states form Gaussian DOS distributions on either side of the carrier energy gap. The more numerous central sites act as transport sites. The deep tail sites act as continuous, pseudo-exponential trap distribution. Chemical impurities or structural defects form relatively discrete, isoelectronic trapping level in the carrier energy gap.

Theoretically the trap characteristics (density and energy) can be included in the *J-V* model and extracted experimentally. By considering the Poisson equation together with the total current equation:[11]

$$\frac{dE(x)}{dx} = q\left[n(x) + n_t(x)\right] / \varepsilon_r \varepsilon_0 \tag{2.1}$$

$$J = q\mu_{dc} n(x) E(x) \tag{2.2}$$

along with the boundary condition,

$$V = \int_0^L E(x)dx \tag{2.3}$$

where $E(x)$ is the electric field, L the film thickness, $n(x)$ the mobile carrier density, q the electron charge and $n_t(x)$ the trapped carrier density. Assuming $n_t(x)$ is much larger than $n(x)$ and approximating the Fermi occupancy function by a step function. For the exponentially distributed traps $h(E)$,

$$h(E) = \frac{H_t}{E_t}\exp\left(-\frac{kT}{E_t}\right) \tag{2.4}$$

The final solution for J-V characteristics can be written as [11].

$$J = N\ \mu_{dc} q^{(1-l)}\left[\frac{\varepsilon_r \varepsilon_0 l}{H_t(l+1)}\right]\left(\frac{2l+1}{l+1}\right)^{(l+1)} \frac{V^{(l+1)}}{L^{(2l+1)}} \tag{2.5}$$

Here, N is the density of state, H_t the density of traps, L is the film thickness and $l = E_t / kT$ where E_t is the characteristic trap energy. By plotting ln J versus ln V, the slope is equal to $l+1$ and the E_t can be extracted. After that the value of H_t can be figured out in ln J versus $1000 / T$ plot, where

$$slope = -\frac{E_t}{1000 \times k}\ln\left(\frac{qH_t L^2}{2\varepsilon_r \varepsilon_0 V}\right) \tag{2.6}$$

Here k is the Blotzmann's constant.

2.1.3 Metal/organic interface

Metal electrodes are commonly used in most organic devices, and their performance and even the life time are mainly determined by metal-organic interaction and carrier injection efficiency at the interface. Therefore numerous of studies have been done to understand the interfacial effects [12-19].

Due to the weak Van der Waals intermolecular bonding, organic molecular

semiconductor interfaces had been expected to form weakly interacting boundaries with weak interface bonds and no electronically active defects. Under such conditions, the relative position of molecular levels across the interface would be obtained by simple alignment of the vacuum levels of the two solids, as shown in Fig. 2.3a, which was widely assumed to be correct in the literature on organic devices. However, recent investigations have now firmly demonstrated that this is rarely the case at metal/organic interfaces [12-19]. By using UPS or Kelvin probe, interface dipole barriers with magnitudes greater than 1.0 eV have been found to introduce mis-alignment of vacuum level at the metal/organic interface, as shown in Fig. 2.3b.

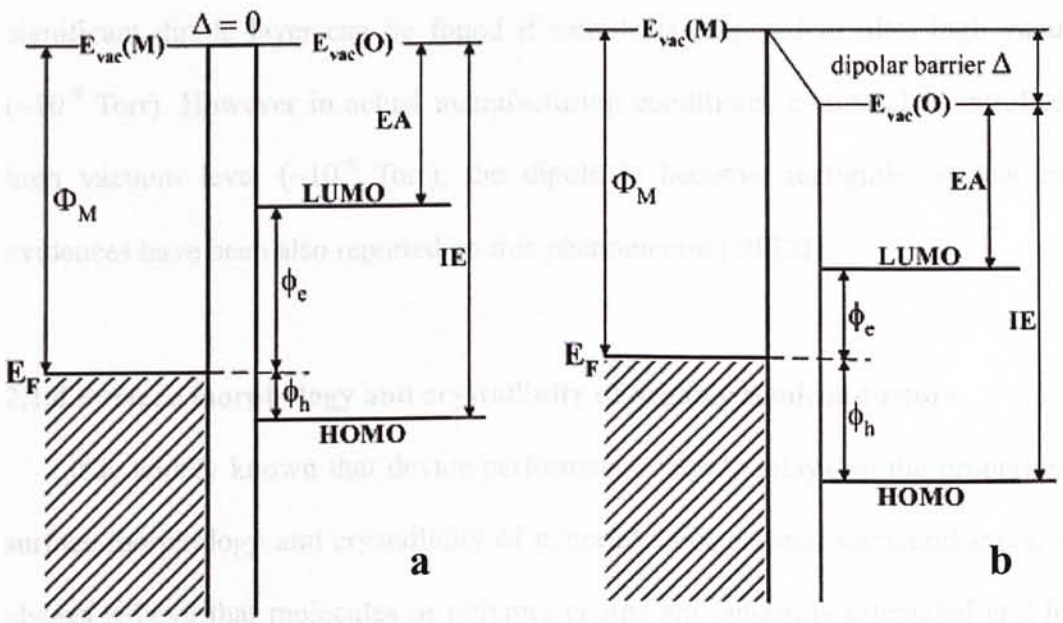

Figure 2.3. Schematic energy diagram of metal-organic semiconductor interface (a) without and (b) with a dipole barrier Δ. ϕ_e and ϕ_h are the electron and hole barriers, and $E_{vac}(O)$ and $E_{vac}(M)$ are the organic and metal vacuum levels, respectively.

Although the dipolar layer just present in the first few monolayer (<10Å) of the organic material and carrier can easily tunneling through, it alters the barrier height at

the interface and eventually alters the carrier injection efficiency. In this case, the energy barrier for carrier injection in the Mott-Schottky model, Eq. 2.7, regarding vacuum level alignment does not hold and should be modified by Eq. 2.8:

$$\phi_h = IE - \Phi_{anode} \quad (2.7a)$$

$$\phi_e = \Phi_{cathode} - EA \quad (2.7b)$$

$$\phi_h = IE - \Phi_{anode} - \Delta \quad (2.8a)$$

$$\phi_e = \Phi_{cathode} - EA + \Delta \quad (2.8b)$$

where ϕ_h and ϕ_e are the barriers for hole and electron injection, respectively.

In fact the value of dipolar layer depends on sample preparation conditions. A significant dipole layer can be found if sample is prepared in ultra high vacuum (~10^{-9} Torr). However in actual manufacturing conditions, commonly controlled in high vacuum level (~10^{-6} Torr), the dipole is become negligible. A few more evidences have been also reported on this phenomenon [20][21].

2.1.4 Surface morphology and crystallinity of organic semiconductors

It is widely known that device performance largely relays on the properties of surface morphology and crystallinity of materials. For organic semiconductors, it is always believe that molecules or polymer chains are randomly orientated and form amorphous thin films [22][23]. In this case, the carriers are scattered at the boundaries of small molecular gains. This is the main cause of extremely low carrier mobility (10^{-9} cm^2/Vs to $1 cm^2/Vs$) in most organic semiconductors [24][25].

Recently attention is paid to increasing the "ordering" of molecules in an organic film. Different chemical and physical approaches have been reported [26-28]. Chemically, novel molecular structures have been synthesized to assist ordering of self-assemble layers. On the other hand, molecular doping or thermal dynamic

approaches are proposed from the view-point of physics. It is successfully demonstrated that by slightly increasing the substrate temperature or post annealing, the gain size is increased and eventually the gain boundaries are reduced. As a result, higher carrier mobility can be achieved. More interestingly, a single crystal of organic thin film has also been applied in field effect transistors (FETs) with a carrier mobility larger than 10 cm^2/Vs [29-31]. Single crystal is believed to be the upper limit of the carrier mobility that the material can be reached.

Experimental

2.2.1 Experimental scheme

The experimental approach in this chapter is to investigate the surface morphology and crystallinity changes under various substrate temperatures. It is then followed by using variable temperature *J-V* technique to extract the trap density in Au/CuPc/Au devices. For electrical measurements, the samples are characterized in a vacuum chamber with 10^{-2} Torr base pressure.

2.2.2 Sample preparation

To investigate the substrate temperature effects, phthalocyannie (CuPc) molecules were thermally evaporated on a quartz substrate which was mounted on a heater. The temperature was precisely controlled with a fluctuation smaller than $\pm 3^{o}C$. For electrical measurements, the device structure under investigation consists of a single layer of CuPc thin film sandwiched by two gold electrodes on the quartz substrate. The HOMO level of CuPc is reported at about 4.8 eV, therefore, the high work function of gold (5.1 eV) can ensure unipolar injection of holes from the electrodes. High purity of CuPc has been purchased from Zencatec Co. without further purification. Au was procured from Aldrich Co. at the highest purity available. The Au electrodes and CuPc thin films were thermally evaporated though shadow masks inside a vacuum chamber at a base pressure of $2\text{-}3\times10^{-6}$ Torr. In order to ensure the film uniformity, the distance between the source and substrate was separated by at least 20 cm and the evaporation rate was monitored at 0.3-0.5 Å/s.

2.3 Data analysis and discussions

2.3.1 Surface morphology on substrate temperature effect

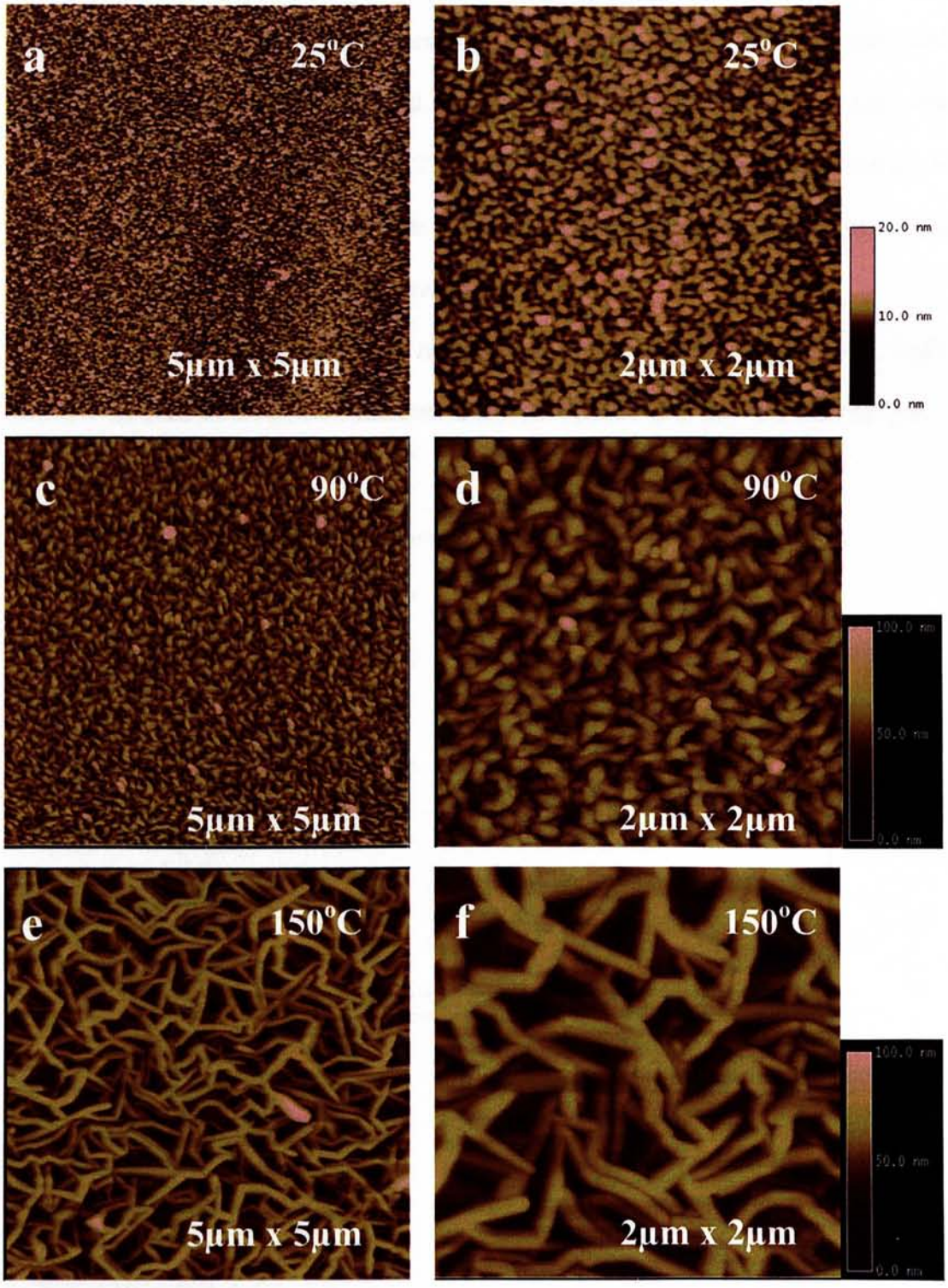

Figure 2.4. AFM images of 200nm CuPc thin films on quartz with different substrate temperature (a), (b) 25°C, (c), (d) 90°C, and (e), (f)150°C during evaporation.

In Fig. 2.4, the morphology of CuPc films are changed greatly by increasing the substrate temperature. Small gains with diameter of about 20nm are found for the film grown at 25°C substrate temperature (Fig. 2.4 a, b). The size of gains and roughness are significantly increased for the film grown at 90°C, and the gains are elongated in certain directions (Fig. 2.4 c ,d). The effect of substrate temperature is more clearly shown at 150°C, where nano-size rods are formed with diameter and length about 100nm and a few microns, respectively.

In order to study the substrate temperature effect on the crystallinity of CuPc films, x-ray diffraction (XRD) measurements were carrier out, as shown in Fig. 2.5.

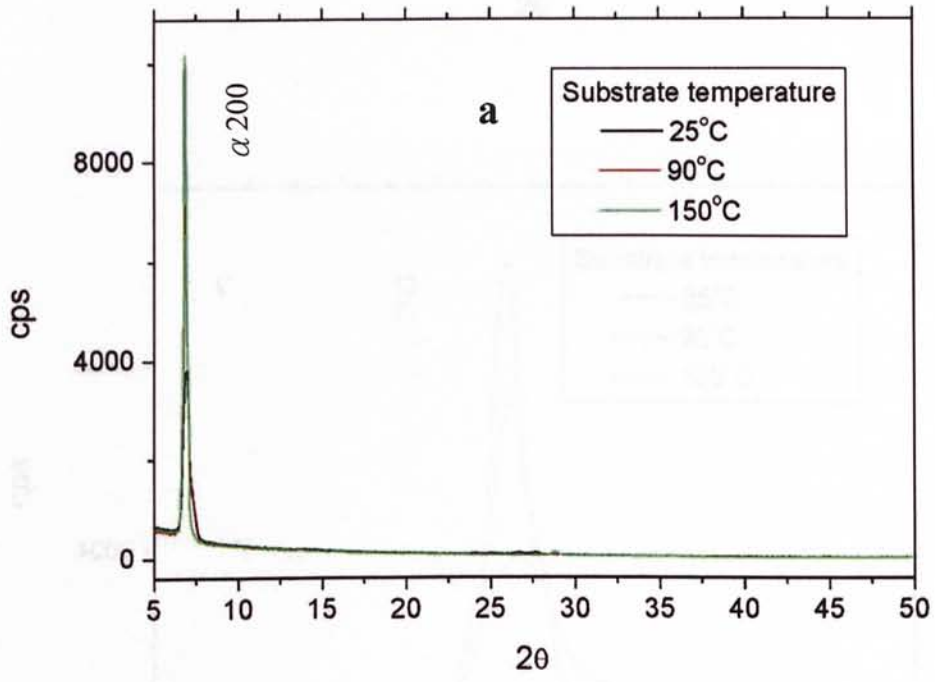

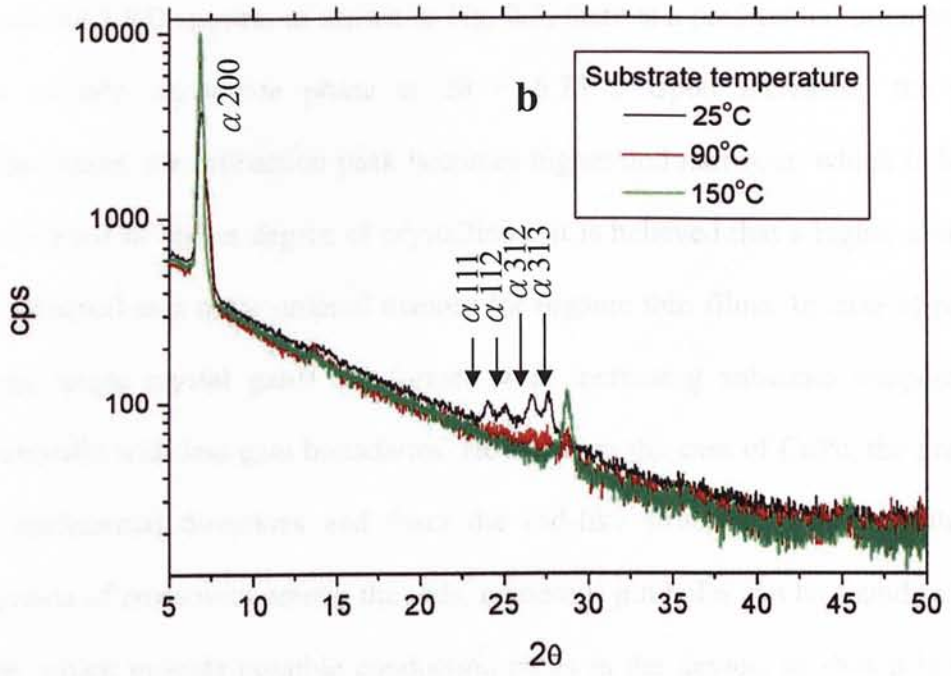

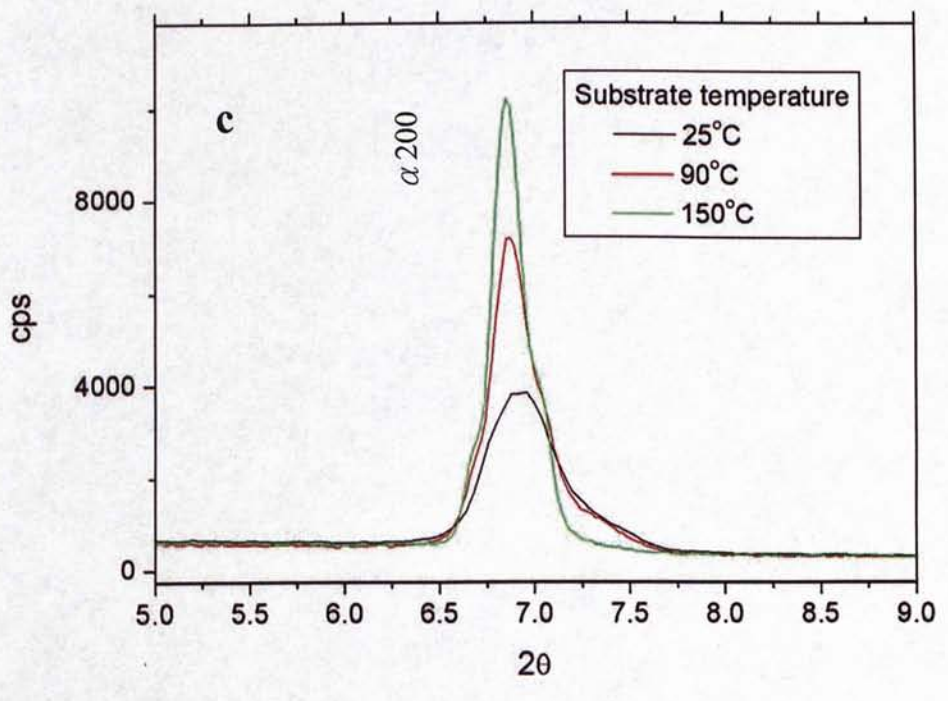

Figure 2.5. XRD spectra of (a) linear and (b)semi-logarithm plots of CuPc films on silicon prepared at different substrate temperatures. Narrow spectra around [200] of crystalline α-CuPc at different temperature at 6.75 ° are shown in Fig. 2.5(c).

It is widely reported that α phase CuPc is form by thermal evaporation [32-34]. From the XRD spectra, as shown in Fig. 2.5, there is a preferential orientation [200] for α-CuPc crystalline phase at $2\theta = 6.75^{\circ}$. Upon increasing the substrate temperature, the diffraction peak becomes higher and narrower, which indicates the occurrence of higher degree of crystallinity. It is believed that a higher mobility can be obtained in a more ordered manner for organic thin films. In case of pentacene, large single crystal gains are formed with increasing substrate temperature and eventually with less gain boundaries. However, in the case of CuPc, the grains grow in preferential directions and form the rod-like structure. Therefore there exist myriads of crossovers among the rods, numerous pin holes can be found in the CuPc film which provide possible conduction paths in the device, as shown in the SEM image in Fig. 2.6.

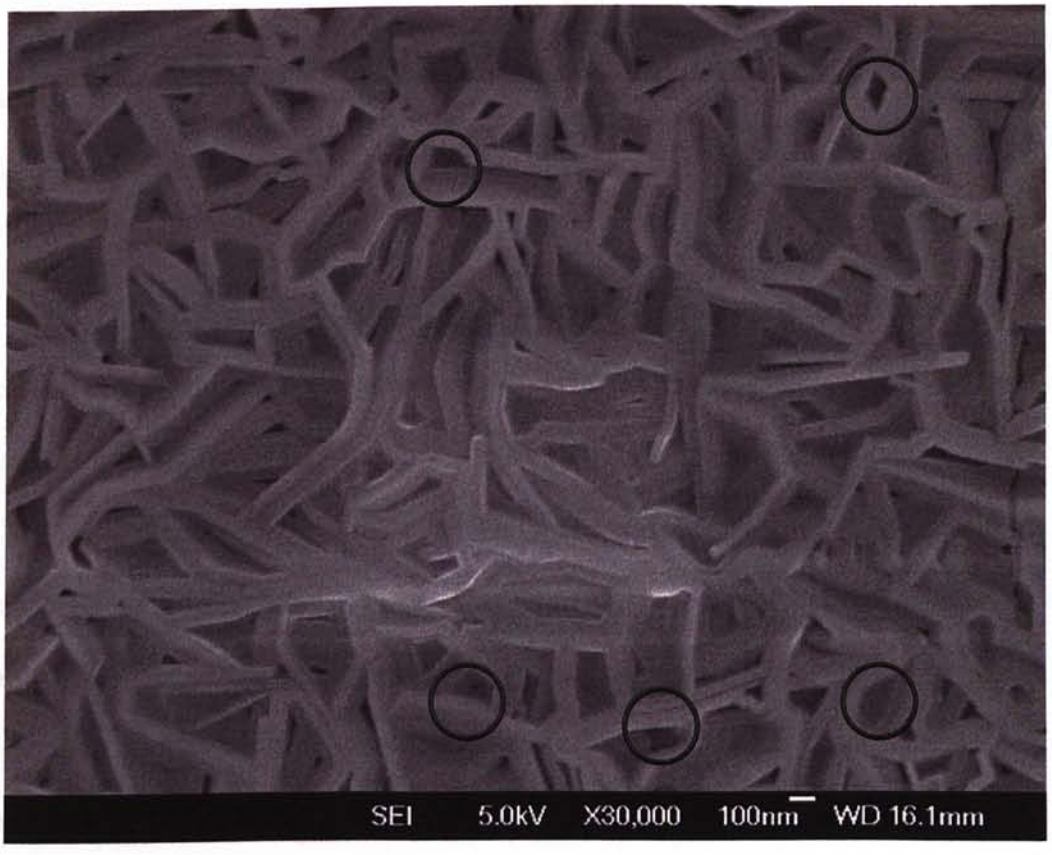

Figure 2.6. SEM image of 200nm CuPc film on silicon with 150°C substrate temperature during evaporation, the circles indicate the locations of the pin holes.

2.3.2 Characteristics of trap in CuPc thin film

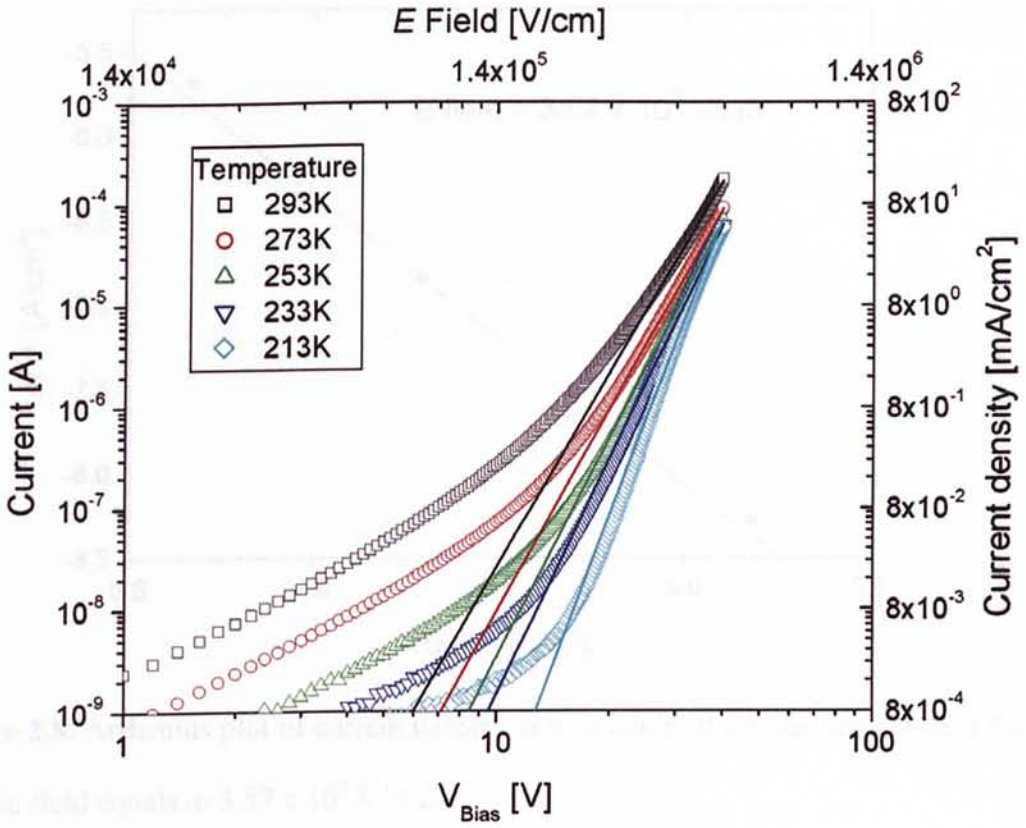

Figure 2.7. *J-V* characteristics of Au/CuPc(700nm)/Au device at different measurement temperatures.

The characteristics of traps in Au/CuPc(700nm)/Au was characterized by variable-temperature *J-V* measurements as shown in Fig. 2.7. In low bias region, less than 10 V, the slope in ln J v.s. ln V plot is less than two, which is corresponding to *SCLC* with traps region. On the other hand, the current increases rapidly with slope greater than ten in high bias region. This rapid increase of current is attributed to the trap filling region. In most organic systems, exponential distribution of traps is commonly found, which is characterized by the characteristic trap energy E_t and trap density H_t. According to Eq. 2.4 and Eq. 2.5, the slope of the *ln J* versus *ln V* plot is equal to $l+1$, here $l = E_t kT$ with E_t be the characteristic trap energy. By extracting the slope at the high bias region in Fig. 2.7, we get $E_t = 0.14 \pm 0.1\, eV$.

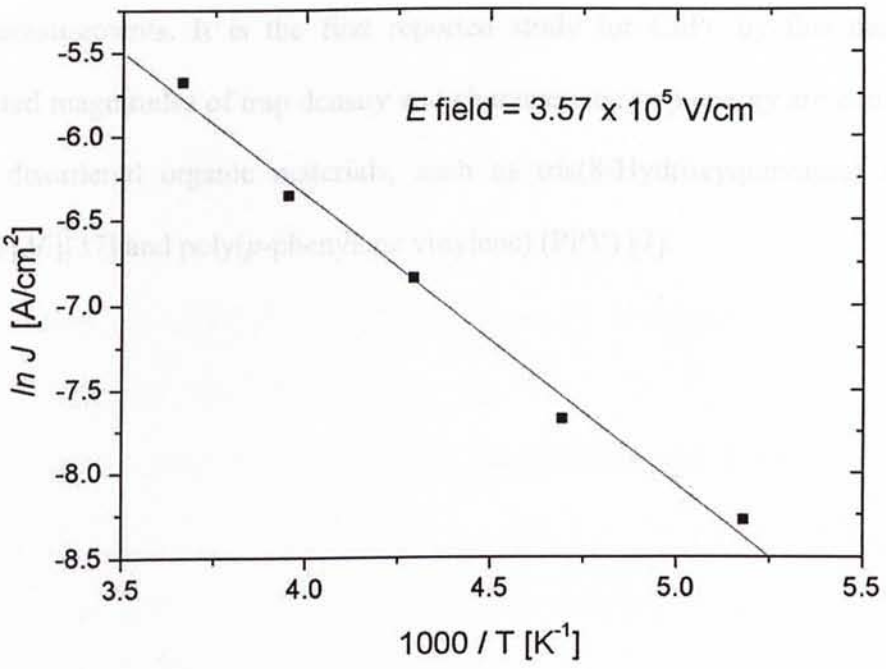

Figure 2.8. Arrhenius plot of current density as a function of inverse temperature for electric field equals to 3.57 x 10^5 V/cm.

As described in Eq. 2.6, the trap density H_t can be extracted from the slope of the ln J versus 1000 / T plot at a fixed field strength. From the fitting shown in Fig. 2.8, we obtain $H_t = (5.42 \pm 0.34) \times 10^{16}$ cm^{-3}. The order of magnitudes of H_t and E_t obtained for CuPc film in commonly found in other disordered organic material systems [7-10][35][38].

2.4 Conclusions

The morphology and crystallinity of CuPc thin films are largely depended on the substrate temperature during evaporation. If the temperature is high enough, single crystalline nano-rods of CuPc can be obtained. However the high temperature treatment also results in very rough surface morphology. This makes difficult to implement into device fabrication. On the other hand, it has been successfully

demonstrated that the trap characteristics of CuPc extracting by variable-temperature *J-V* measurements. It is the first reported study for CuPc by this method. The extracted magnitudes of trap density and characteristic trap energy are comparable to other disordered organic materials, such as tris(8-Hydroxyquinoline) Aluminum (Alq_3) [36][37] and poly(*p*-phenylene vinylene) (PPV) [7].

Reference

[1] The Nobel Prized in Chemistry, 2000, www.nobel.se/chemistry/laureates/2000

[2] N. C. Greenham and R. H. Friend, Solid State Phys. **49** (1995).

[3] C. E. Swenberg and M. Pope, *Electronic Processes of Organic Crystals and Polymers*, Oxford University Press, Oxford (1999).

[4] P. M. Borsenberger and D. S. Weiss, *Organic Photoreceptors for Xerography*, Marcel Dekker, New York (1998).

[5] L. J. Rothberg and A. J. Lovingerm, J. Materials Research **11**, 3174 (1996).

[6] R. Hoffmann, C. Janiak, and C. Kollmar, Macromolecules, **24**, 3725 (1991).

[7] A. J. Campbell, D. D. C. Bradley, and D. G. Lidzey, J. Appl. Phys. **82**, 6326 (1997).

[8] B. Ries, H. Bassler, M. Grunewald, and B. Movaghar, Phys. Rev. B **37**, 5508 (1988).

[9] Rashmi, V. R. Balakrishnan, A. K. Kapoor, V. Kumar, S. C. Jain, R. Mertens, and Annapoorni, J. Appl. Phys. **94**, 5302 (2003).

[10] S. C. Jain, A. K. Kapoor, W. Geens, J. Poortmans, R. Mertens, and M. Willander, J. Appl. Phys. **92**, 3752 (2002).

[11] K. C. Kao and W. Hwang, *Electrical Transport in Solids* (Pergamon, Oxford, U.K., 1981).

[12] N. Koch, A. Elschner, J. Schwartz, and A. Kahn, Appl. Phys. Lett. **82**, 2281 (2003).

[13] C. Shen, A. Kahn, J. Schwartz, J. Appl. Phys. **90**, 6236 (2001).

[14] L. Yan, M. G. Mason, C. W. Tang, Y. Gao, Appl. Surf. Sci., **175-176**, 412-418 (2001).

[15] H. Ishii, K. Sugiyama, E. Ito, and K. Seki, Adv. Mater. **11**, 605 (1999).

[16] I. Hill, A. Rajagopal, A. Kahn, and Y. Hu, Appl. Phys. Lett. **73**, 622 (1998).

[17] I. Hill, A. Rajagopal, and A. Kahn, J. Appl. Phys. **84**, 3236 (1998).

[18] S. T. Lee, X. Y. Hou, M. G. Mason, and C. W. Tang, Appl. Phys. Lett. **72**, 1593 (1998).

[19] I. G. Hill, A. J. Makinen, and Z. H. Kafafi, J. Appl. Phys. **88**, 889 (2000).

[20] G. Greczynski, Chem. Phys. Lett. 321, 379 (2000).

[21] G. G. Malliaras, J. R. Salem, P. J. Brock, J. C. Scott, Phys. Rev. B 58, R13411 (1998).

[22] E. Han, L. Do, M. Fujihira, H. Inada, and Y. Shirota , J. Appl. Phys. **80**, 3297 (1996).

[23] M. A. Baldo and S. R. Forrest, Phys. Rev. B **64**, 085201 (2001).

[24] C. D. Dimitrakopoulos and D. J. Mascaro, IBM J. Res. & Dev. **45**, No.1 (2001).

[25] C. D. Dimitrakopoulos and P. R. L. Malenfant., Adv. Mater. **14**, No.2 (2002)

[26] Christopher R. Newman, Reid J. Chesterfield, Jeffrey A. Merlo, and C. Daniel Frisbie, Appl. Phys. Lett. **85**, 422 (2004).

[27] Takeo Minari, Takashi Nemoto, and Seiji Isoda, J. Appl. Phys. **96**, 769 (2004).

[28] Jiyoul Lee, J. H. Kim, and Seongil Im, J. Appl. Phys. **95**, 3733 (2004).

[29] Oana D. Jurchescu, Jacob Baas, and Thomas T. M. Palstra, Appl. Phys. Lett. **84**, 3061 (2004)

[30] V. C. Sundar et al., Science **303**, 1644 (2003).

[31] V. Podzorov et al., Cond. Mat. 0403575.

[32] M. Nakamura, Y. Morita, Y. Mori, A. Ishitani, and H. Tokumoto, J. Vac. Sci. Technol. B **14(2)**, 1109 (1996).

[33] R. Resel, M. Ottmar, M. Hanack, J. Keckes, and G. Leising, J. Mater. Res., **15**, 934 (2000).

[34] O. Berger, W. J. Fischer, B. Adolphi, S. Tierbach, V. Melev, and J. Schreiber, J. Mater. Sci., **11**, 331 (2000).

[35] V. Kumar, S. C. Jain, A. K. Kapoor, W. Geens, T. Aernauts, J. Poortmans, and R. Mertens, J. Appl. Phys. **92**, 7325 (2002).

[36] P. Burrows, Z. Shen, V. Bulovic, D. McCarty, S. Forrest, J. Cronin, and M. Thompson, J. Appl. Phys. 79, 7991 (1996).

[37] W. Brütting, S. Berleb, and A. Mückl, Org. Electron. 2, 1 (2001).

[38] V. Kumar, S. C. Jain, A. K. Kapoor, J. Poortmans, and R. Mertens, J. Appl. Phys. **94**, 1283 (2003).

Chapter 3

CHARGE TRANSPROT IN CuPc ORGANIC SEMICONDUCTOR

Abstract

This chapter begins with the physics of carrier injection and transport in organic semiconductors. The Scher-Montroll model for dispersive transport will then be introduced, and followed by highlighting the Gaussian disorder model in energetic and structural disorder systems. Detailed experimental works based on admittance spectroscopy on carrier transport in CuPc organic semiconductor will be presented as well.

3.1 Introduction of charge transport in organic semiconductors

The maximum current density that can pass through a trap-free, depleted semiconductor with thickness L is given by the Mott-Gurney law[1], i.e., the space-charge-limited current (SCLC):

$$J_{SCLC} = \frac{9}{8}\varepsilon\mu_{dc}\frac{V^2}{L^3} \tag{3.1}$$

where ε is the dielectric constant and μ_{dc} is the average carrier mobility. In the case of field and temperature dependent mobility, Gill [2] proposed an empirical law for carrier mobility in this class of materials according to:

$$\mu_{dc}(T,E) = \mu_0 \exp\left[-\frac{\Delta}{k_B T} + B\left(\frac{1}{k_B T} - \frac{1}{k_B T_0}\right)\sqrt{E}\right] \tag{3.2}$$

This field and temperature dependent mobility has been observed in a large number of disordered molecular materials [3].

3.1.1 Carrier injection at metal/organic interface

The major concern of the carrier injection from a metal electrode to an organic semiconductor is the injection efficiency η, which is the ratio between the injected current J_{INJ} and J_{SCLC} [4].

$$\eta = \frac{J_{INJ}}{J_{SCLC}} \tag{3.3}$$

For an Ohmic contact, the injection efficiency is 1 and the current is limited by the

carrier mobility in the bulk. If the contact is not Ohmic, then the current is limited by the injection. The injection efficiency is less than 1 for an injection-limited contact.

The metal/organic energy profile therefore is important to determine the injection efficiency. Although formation effects have been reported for contacts made by evaporating a metal on an organic thin film and certain metal even has been found to react with some organic semiconductor [5][6][7], the energy barrier at the interface is generally found to be scaled with the difference in the appropriate energy levels of the metal and the organic. Intensive efforts have been made on the investigation of injection efficiency with different metal and organic composites [8][9].

In a simple thermal ionic emission model, the current does not depend on the mobility. However, for low mobility materials, thermal ionic current has been analytically determined by Emtage and O'Dwyer [10]. Afterwards, Scott and Malliaras have extended the theory by considering injection and recombination flux [11]. It was found that the current is proportional to the carrier mobility in organic semiconductor:

$$J_{INJ} = 4\psi^2 N_0 e\mu_{dc} E \exp\left(\frac{-\phi_B}{kT}\right)\exp\left(f^{1/2}\right) \tag{3.4}$$

where ψ is a slowly varying function of electric field, N_0 is the density of hopping sites, f is a function of electric field, and ϕ_B is the Schottky energy barrier. The last exponential function represents the Schottky barrier lowering effect with the applied field.

3.1.2 Carrier transport in organic semiconductors

In inorganic semiconductors (e.g. Si, GaAs etc.), strong covalent bonds hold atoms together with well ordered configurations. The energy band in this case extends continuous in the bulk and therefore the carriers can freely move in the band with a relative high mobility. However, for most of organic semiconductors, week intermolecular force (Van der Waals force) is predominant among molecules or polymers. In this case, discrete energy band structure is dominant in the bulk, as shown in Fig. 3.1. As a result, carrier transport in organic semiconductors is a hopping process that involves tunneling of carriers among localized states with a mean-free path much smaller than the intermolecular distance [12].

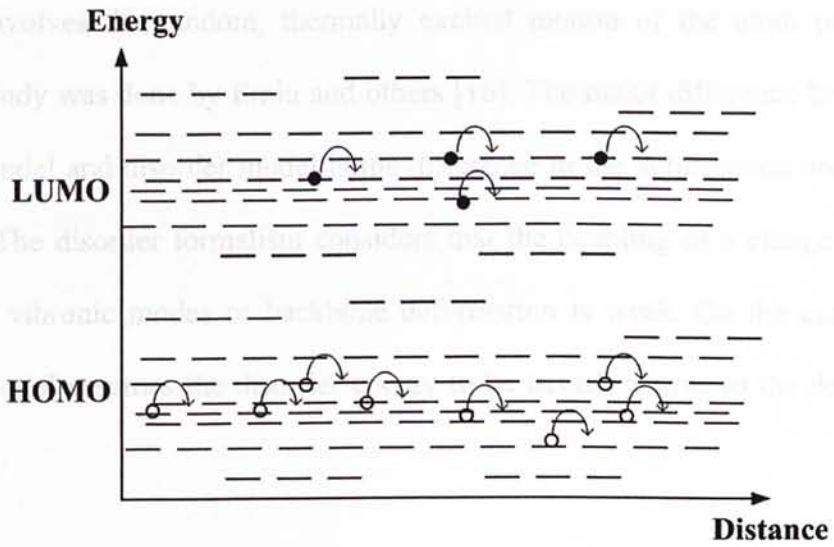

Figure 3.1. Energy band structure in organic semiconductor with electrons and holes hopping across discrete energy levels in *LUMO* and *HOMO,* respectively.

By considering the hopping energy, distance among sites, applied electric field and polarizability of the material etc., the hopping rate can be determined by modeling those parameters. A few approaches have been proposed to model the

carrier transport in organic semiconductors, i.e. the polaron model [13], the Scher-Montroll model [14], and the Gaussian disorder model [15].

3.1.2.1 Polaron model

When a carrier is localized in a hopping site as it is being transported in the organic semiconductor, the excess charge may cause a displacement in the position of the surrounding molecules. In this case, the hopping carrier does not move as a free particle. Instead it has to drag a deformation cloud surrounded around itself. The resulting particle that includes the carrier and its deformation cloud, is called a polaron [13].

Polaron motion requires molecular displacements. The mechanism of the process involves the random, thermally excited motion of the atom position. A detailed study was done by Emin and others [16]. The major difference between the polaron model and disorder model is the difference in the deformation and disorder energies. The disorder formalism considers that the coupling of a charge carrier to molecular vibronic modes or backbone deformation is weak. On the contrary, the polaron model assumes the disorder energy to be trivial relative to the deformation energy.

3.1.2.2 Scher-Montroll model – Anomalous dispersive transport

Charge transport can be viewed as an accumulated sequence of charge transfer steps from one localized site to the other. In this case, each carrier independently undergoes a random walk, biased into one direction by an applied electric field. The entire character of a propagating packet of carriers depends on a key feature, the hopping time probability distribution $\psi(t)$. In an ordered single crystal, where the

hopping rate W is constant, $\psi(t)$ is given by [17].

$$\psi(t) \propto \exp(-Wt) \tag{3.5}$$

and the charge packet exhibits a normal Gaussian transport. Diffusive spreading of charge packet causes some broadening of the trailing edge in the case of photocurrent transient. As long as the field is small and the material is homogeneous, [18] Einstein's law holds so that $D = \mu \frac{kT}{q}$. In this case the spatial width of the charge sheet evolves as:

$$\left\langle (x - x_0)^2 \right\rangle^{1/2} = (2Dt)^{1/2} \tag{3.6}$$

In disordered systems, however, there is a wide distribution of hopping rates, leading to a large range of hopping times that extend well in to the experimental time scale. In this case, the probability distribution becomes:

$$\psi(t) \propto t^{-(1+\alpha)} \quad , \quad 0 < \alpha < 1 \tag{3.7}$$

proposed by Scher and Montroll [14], has been very successful in describing TOF experiments in organic and amorphous semiconductors. Such a probability distribution implies an extremely large hopping time dispersion which can result from relatively small variations between the distance and the mutual orientation of the hopping sites. The mean position $\langle l \rangle$ of a spatially biased, time-evolving packet of charge carriers that undergoes a random walk with a probability distribution like

one described by Eq. 3.7 varies as:

$$\langle l \rangle \propto t^{\alpha} \tag{3.8}$$

The parameter α measures the degree of disorder [19]. When $\alpha \to 1$, the mean position of $\psi(t)$ increases linearly with time, as in the case of Gaussian transport. A smaller α is associated with higher degree of disorder.

In conventional time-of-flight (TOF) experiments, the current measured before the packet reaches the opposite electrode is governed by:

$$J(t) \propto \frac{d\langle l \rangle}{dt} \propto t^{-(1-\alpha)} \tag{3.9}$$

and it is no longer constant, but it is decreasing with time. When carriers begin to reach the opposite electrode and become annihilated, a fast drop in the current is observed:

$$J(t) \propto t^{-(1+\alpha)} \tag{3.10}$$

According to Eqs. (3.9) and (3.10), the shape of the TOF trace is described by only on parameter. When plotted in a double logarithmic scale, it consists of two lines with slopes $-(1-\alpha)$ and $-(1+\alpha)$, crossing at a time that corresponds to the arrival time. A typical TOF profile as shown in Fig. 3.2.

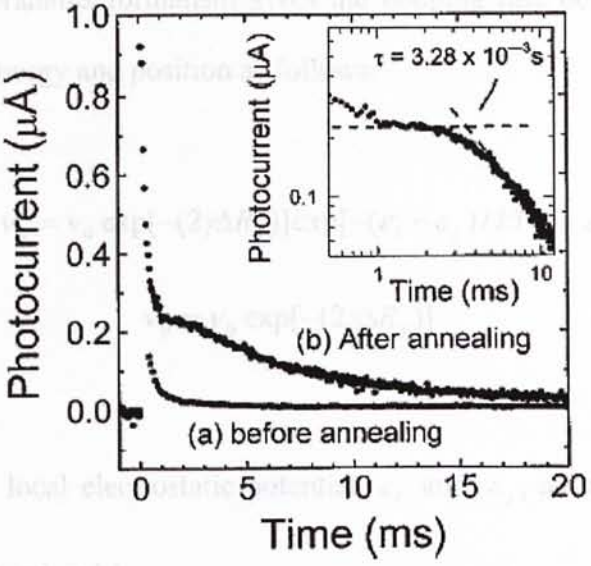

Figure 3.2. A typical TOF profile, by S. C. Tse, H. H. Fong, and S. K. So in J. Appl. Phys. **94**, 2033 (2003).

3.1.2.3 Gaussian disorder model

The Gaussian disorder model proposed by Bässler including the effects of both energetic disorder, structural disorder and polaronic effects. Energetic disorder arises from the random distribution of permanent dipoles and the randomly induced charge fluctuations associated with intermolecular forces. This disorder introduces the fluctuations to the energy level of sites, splitting the transport states into a distribution of localized states. These two contributions to the energetic disorder can be treated by exploiting the Gaussian distribution, whose variance can be included.

Structure or positional disorder originates from the fluctuations in the intermolecular distance and mutual orientation of molecules nearby, as well as the overlapping of the orbital of sites *i* and *j* is concerned. The probability of a hop between sites *i* and *j* exponentially depends on their separation. Transport is therefore considered as the hopping of carriers in a Gaussian distribution of the localized states.

The Miller-Abrahams formalism gives the hopping rate between sites i and j with difference in energy and position as follows:

$$\nu_{ij} = \nu_0 \exp[-(2\gamma\Delta R_{ij})]\exp[-(\varepsilon_i - \varepsilon_j)/kT] \quad \varepsilon_i > \varepsilon_j \tag{3.11}$$

$$\nu_{ij} = \nu_0 \exp[-(2\gamma\Delta R_{ij})] \quad \varepsilon_i < \varepsilon_j \tag{3.12}$$

which includes the local electrostatic potential ε_i and ε_j, as well as the intersite distance between sites i and j.

By considering the energetic relaxation, it was analytically shown that the carriers relax to an average energy level below the mean energy of the Gaussian distribution by $-\sigma^2/kT$. As a result, hopping occurs among the tail states of the Gaussian density of states (DOS). Due to the asymmetry of the hopping rate, Mote Carlo simulations were used to determine the transport properties, with the additional assumption that the energies of adjacent sites are uncorrelated. The mobility in this case is expressed as:

$$\mu = \mu_0 \exp\left[-\frac{2\hat{\sigma}^2}{3} + C(\hat{\sigma}^2 - \Sigma^2)\sqrt{E}\right] \quad \text{for } \Sigma \geq 1.5 \tag{3.13a}$$

$$\mu = \mu_0 \exp\left[-\frac{2\hat{\sigma}^2}{3} + C(\hat{\sigma}^2 - 1.5^2)\sqrt{E}\right] \quad \text{for } \Sigma < 1.5 \tag{3.13b}$$

where $\hat{\sigma} = \sigma/kT$, $\Sigma/\sqrt{2}$ is the standard deviation of the Gaussian positional distribution, and C is a constant.

This model is widely used to analyze the charge transport properties in organic

semiconductors and proved in good agreement with experimental data. By figuring out the distribution parameter σ, it is able to quantitatively study the disorder effect in charge transport in different material systems.

3.2 Experimental

3.2.1 Experimental Scheme

In this chapter, a unique characterization technique, admittance spectroscopy is employed to study the carrier transport properties and dispersivity in copper phthalocyannie (CuPc) organic solid film. To minimize the influence of interfacial effect and ensure only hole injection, a high work function of metal-Au is chosen as the electrodes. The results are further evaluated by a complementary experiment, dark-injection space-charge-limited transient current measurement.

3.2.2 Sample preparation

For electrical measurements, the device structure under investigation consists of a single layer of copper phthalocyannie (CuPc) thin film sandwiched by two gold electrodes on a quartz substrate. The HOMO level of CuPc is reported at about 4.8 eV, the high work function of gold (5.1 eV) can ensure unipolar injection of holes from the electrodes. Highly pure CuPc was purchased from Zencatec Co. without further purification. Au was procured from Aldrich with the highest purity available. The Au electrodes and CuPc thin films were thermally evaporated though shadow masks inside a vacuum chamber at a base pressure of $2\text{-}3\times10^{-6}$ Torr. In order to ensure the film uniformity, the distance between the source and substance was separated by at least 20 cm and the evaporation rate was controlled at 0.3-0.5 Å/s.

3.2.3 Admittance spectroscopy

Admittance spectroscopy is a powerful technique to investigate charge transport kinetics and relaxation processes involved in solid state electron devices[20]. Here we study the capacitance of hole-only Au/CuPc/Au device as a function of frequency

$f = \omega / 2\pi$, where

$$C(\omega) = \mathrm{Im}(Y / \omega) \tag{3.14}$$

and Y is the admittance of the devices.

In the space-charge-limited current (SCLC) regime, the device modulation voltage v_{ac} can be used to probe the existing space charge in the device and inject new carriers [21][22]. The time scale for building up additional space-charge is given by the transit time τ_t of the injected carriers. At frequencies $\omega<\tau_t^{-1}$, the extra carriers lead to an additional current, which lags behind the ac stimulus. Since $Y = i_{ac} / v_{ac}$, the decreasing phase of Y means an apparently inductive contribution to the capacitance. At high frequencies, the period of the applied ac field is too short to redistribute the space-charge in the device. In this case, the inductive contribution to the admittance disappears and the measured capacitance equals the geometrical value, $C_{geo} = \frac{\varepsilon_r \varepsilon_0 A}{L}$. The mechanism is illustrated in Fig. 3.3.

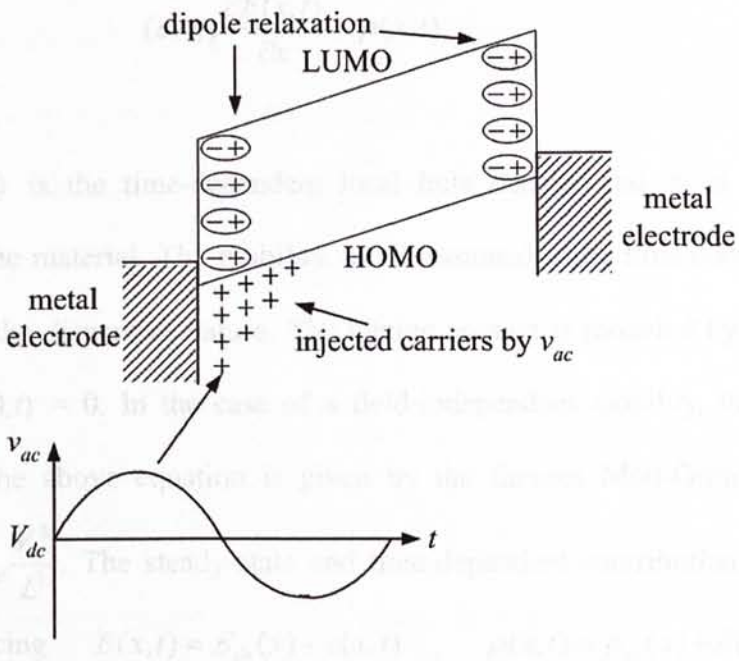

Figure 3.3. Schematic diagram of carrier relaxation under ac modulation voltage.

Due to disorder nature in most organic solid films, the transit time of individual carriers is strongly dispersed. As the finite transit time of injected carriers gives rise to an inductive contribution to the admittance, the distribution of transit times will be reflected in the frequency-dependent electrical response of the device.

Theoretical model based on the time-dependent injection of the space-charge-limited current has been successfully applied by Martens et al.[21] to hole transport in the electroluminescent polymer-poly(phehylenevinylene) (PPV). Afterwards, Stefan Berleb and Wolfgang Brütting [22] modified it with the considerations of field-dependent electron mobility and trapping in tris(8-hydroxyquinoline) aluminum (Alq_3). According to Martens's approach, the time-dependent injection of the space-charge-limited current is described by the total current equation and the Poisson equation:

$$J(t) = q\rho(x,t)\mu(t)E(x,t) + \varepsilon\frac{\partial E(x,t)}{\partial t} \tag{3.15}$$

$$(\varepsilon / q)\frac{\partial E(x,t)}{\partial x} = \rho(x,t) \tag{3.16}$$

where $\rho(x,t)$ is the time-dependent local hole density and ε is the dielectric constant of the material. The mobility μ is assumed to be time-dependent, which results from the dispersive nature. The Ohmic contact is modeled by the boundary condition $E(0,t) = 0$. In the case of a field-independent mobility, the steady-state solution of the above equation is given by the famous Mott-Gurny square law, $J_{SCLC} = \frac{9}{8}\varepsilon\mu_{dc}\frac{V^2}{L^3}$. The steady-state and time-dependent contribution are separated by introducing $E(x,t) = E_{dc}(x) + e(x,t)$, $\rho(x,t) = \rho_{dc}(x) + \delta(x,t)$, and

$J(x,t) = J_{dc} + j(x,t)$. By solving Eq. (3.15) and (3.16), gives:

$$q\mu(t)\rho_{dc}e(x,t) + \varepsilon\mu(t)E_{dc}\frac{\partial e(x,t)}{\partial x} + \varepsilon\frac{\partial e(x,t)}{\partial t} = j(t) \tag{3.17}$$

The first term in Eq. (3.17) on the left-hand side describes the response of the "background" charge density in the device. The secosnd term gives the current due to the additional time-dependent injected charge-carrier density. The last contribution stems from the dielectric displacement. By applying the Fourier transform to the above equation, as shown in *Appendix A*, an analytical solution of the field-independent mobility and the complex admittance Y is obtained [21]:

$$Y(\Omega) = \frac{\varepsilon A}{L\tau_t}\frac{\Omega^3}{2i(0.75\tilde{\mu})^2[1-e^{-i4\Omega/3\tilde{\mu}}]+1.5\tilde{\mu}\Omega - i\Omega^2} \tag{3.18}$$

with the normalized frequency $\Omega = \omega\tau_t$, and the normalized mobility $\tilde{\mu}(\Omega) = \mu(\Omega)/\mu_{dc}$, where μ_{dc} is the average mobility.

According to the Scher and Montroll (SM) theory [14], dispersive transport is modeled by an algebraically decaying distribution function $\Psi(t) \propto t^{-(1+\alpha)}$ $(0 < \alpha < 1)$, for the waiting time between successive hopes. At short times, the average position $\langle l \rangle \propto t^{\alpha}$ of an injected charge carrier packet is sublinear in time; the mobility $\mu \propto d\langle l \rangle / dt$ decreases with time. At long times, when the carriers have attained equilibrium, the drift velocity is governed by μ_{dc}. The slowing down frequency-dependent mobility equals to $\tilde{\mu}(\Omega) = 1 + M(i\Omega)^{1-\alpha}$ [27], with M a proportionality constant. This kind of dependence is related to the disordered nature

of the materials, which reflects the large spread of waiting times or hopping rates of carriers. Here α and M are measures of dispersivity ($\alpha = 1$ and $M = 0$ for nondispersive transport). In this case, a distribution of transit time is expected to be included. A simple probability distribution function which takes this behavior into account is $P[\ln(\tau_t)] = 1/[\ln(\tau_h) - \ln(\tau_l)] \equiv 1/W$ for $\tau_l \le \tau_t \le \tau_h$ and $P[\ln(\tau_t)] = 0$, for elsewhere [21]. Here τ_l and τ_h correspond to the transit times of the fastest and slowest carriers, respectively. With a proper fitting, the average mobility and dispersive parameter can be obtained.

The impedance measurements were preformed with Hewlett Packard 4284A impedance analyzer. The sweeping frequency of the impedance analyzer ranged from 20 Hz to 1 MHz. To measure the capacitance or conductance, there were two equivalent circuit models in HP 4284A, the parallel and series modes. Owning to large value of impedance (1 kΩ – 5 GΩ) of the capacitor of our devices, the effect of the parallel resistance had relatively more significance than that of series resistance, and the low value of series resistance had negligible significance compared with the capacitive reactance, so the parallel circuit mode was chosen for the measurements. During the measurements, different dc voltages v_{dc} were chosen to superimpose with an ac modulation signal v_{ac}. The capacitance value of the devices is found to be independent of the magnitude of v_{ac}. For each selected dc voltage, a waiting time of 30 seconds was used to stabilize the devices before the data acquisition.

3.2.4 Dark injection space-charge-limited transient current measurements

In the dark injection space-charge-limited transient method, a step voltage is applied to the sample, and the resulting transient current is monitored. If the injection

contact is Ohmic, and the material is trap free, then a characteristic temporal evolution with a maximum is observed. The position of the maximum in time, t_{DI}, is related to the space-charge-free transit time τ_t [1]:

$$t_{DI} = 0.786 \cdot \tau_t \tag{3.19}$$

Therefore the mobility $\mu_{dc} = \frac{L^2}{\tau_t V}$ can be calculated from the position of the maximum current.

Dark injection space-charge-limited (DI-SCL) transient measurements were performed by applying a positive voltage pulse to the one of the Au electrode and measuring the resulting current transient (LeCroy LT264, digital oscilloscope). In order to ensure the injected carriers are fully relaxed before each application of pulse, duty cycle (pulse length / repetition unit) less then 1% was chosen. Fig. 3.4 shows a typical DI SCL transient current trace.

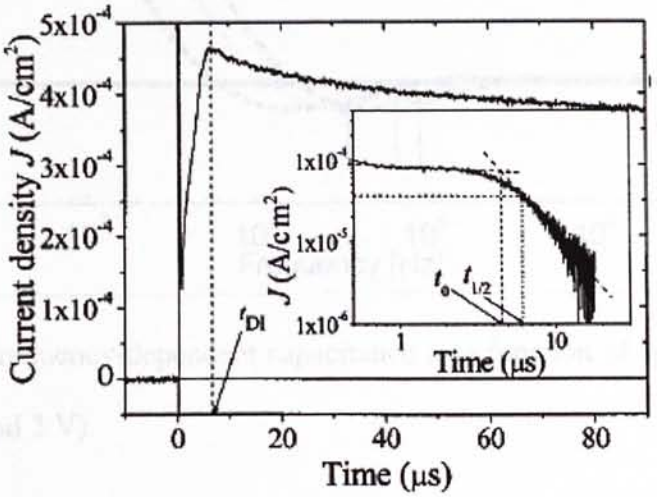

Figure 3.4. A typical DI-SCL transient current trace, the corresponding TOF profile is shown in the inset. D. Poplavskyy, J. Nelson, and D. D. C. Bradley, Appl. Phys. Lett. **83**, 707(2003)

3.3 Results and discussions

3.3.1 Simulation results of admittance spectroscopy

Below are shown a detailed simulation study of the frequency-dependent capacitance under various conditions, e.g., applied bias, mobility, and dispersive parameters.

I. At different applied bias V_{bias}

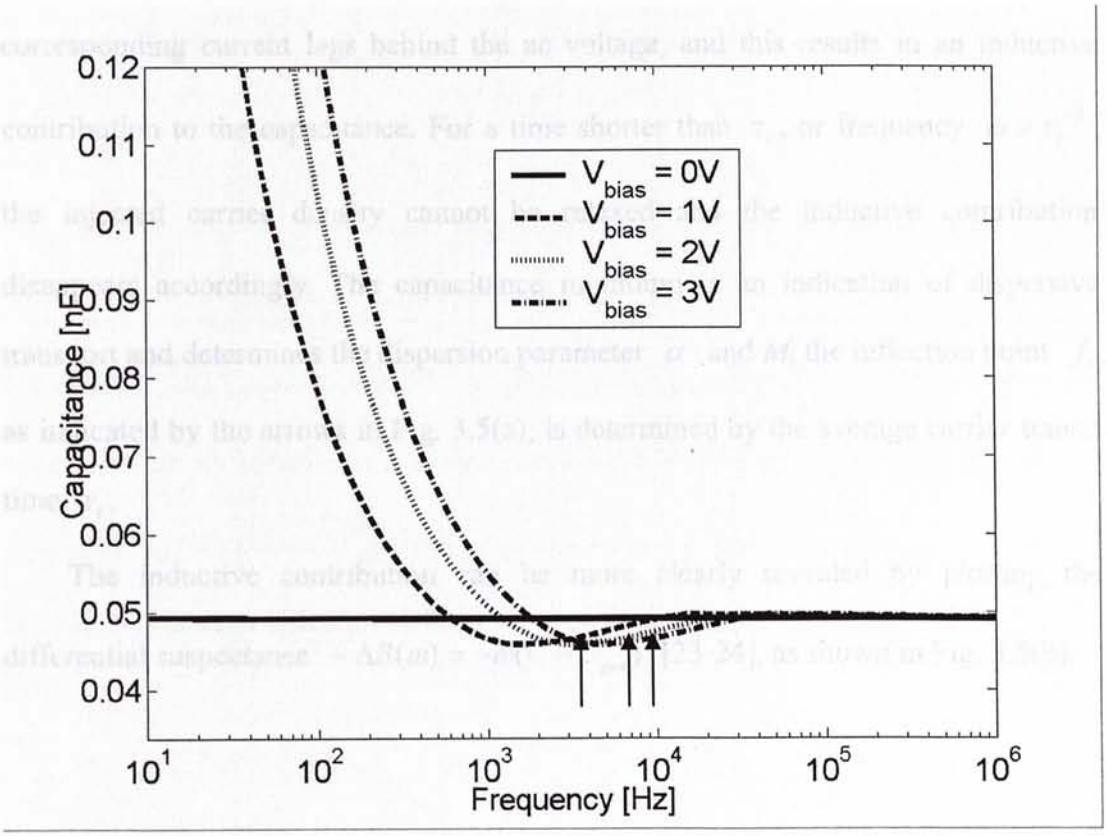

Figure 3.5 (a). Frequency-dependent capacitance as a function of applied bias (V_{bias} = 0 V, 1 V, 2 V, and 3 V).

Table 3.1. Simulation parameters for Fig 3.5 (a).

average mobility μ_{dc}	α	M	ε_r	thickness L	electrode area A
10^{-5} cm^2/Vs	0.6	0.2	2.78	500 nm	10^{-2} cm^{-2}

Fig. 3.5 (a) shows the simulation results from Eq. (3.18) as a function of applied bias, with simulation parameters as shown in Table 3.1. At zero bias the capacitance is independent of frequency, and equal to the geometrical value $C_{geo} = \frac{\varepsilon_r \varepsilon_0 A}{L}$, as expected for an insulating dielectric. However, as the bias is increased, the behavior changes drastically due to the increase of carrier injection. Under the influence of the bias field, the injected carriers move into the device and are relaxed to a new equilibrium of space-charge distribution. Due to the finite transit time τ_t the corresponding current lags behind the ac voltage, and this results in an inductive contribution to the capacitance. For a time shorter than τ_t, or frequency $\omega > \tau_t^{-1}$, the injected carrier density cannot be relaxed and the inductive contribution disappears accordingly. The capacitance minimum is an indication of dispersive transport and determines the dispersion parameter α and *M*, the inflection point f_t, as indicated by the arrows in Fig. 3.5(a), is determined by the average carrier transit time τ_t.

The inductive contribution can be more clearly revealed by plotting the differential suspectance $-\Delta B(\omega) = -\omega(C - C_{geo})$ [23-24], as shown in Fig. 3.5(b).

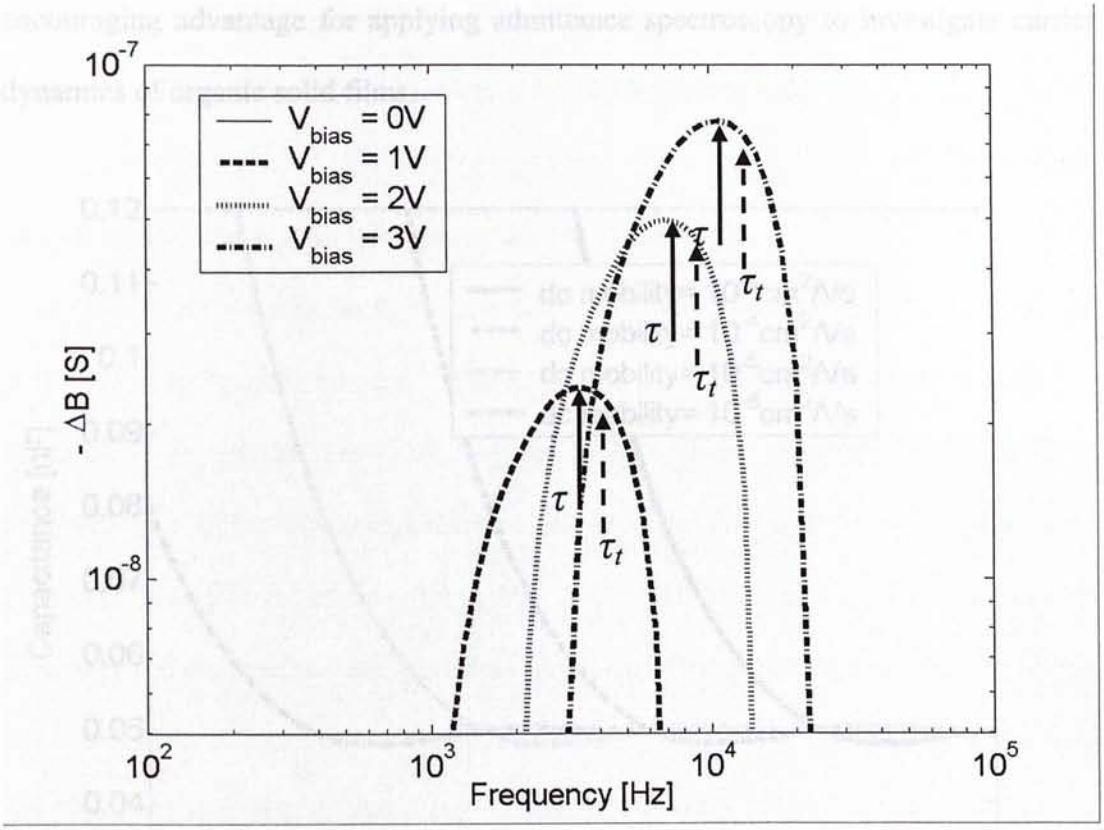

Figure 3.5 (b). Double-logarithmic plot of the negative differential suspectance versus frequency at different bias voltage $-\Delta B(\omega) = -\omega(C - C_{geo})$ from Fig. 3.5(a). The solid arrows (⟶) and dotted arrows (- - - -▸) represent the relaxation τ and transit τ_t times, respectively.

In Fig. 3.5 (b), the transit time τ_t is located at the rising edge of $-\Delta B$ in the high frequency side, which is related to the relaxation time τ at maximum of $-\Delta B$ by a factor $\kappa \geq 1$, i.e. $\tau \approx \kappa \times \tau_t$. The value of κ depends on the dispersivity of carriers, where $\kappa = 1$ for non-dispersive transport.

II. With different mobility μ_{dc}

Most of carrier mobility in organic solids are range from 10^{-8} cm^2/Vs to 1 cm^2/Vs. This is within the detection limit of conventional analyzers, which is an

encouraging advantage for applying admittance spectroscopy to investigate carrier dynamics of organic solid films.

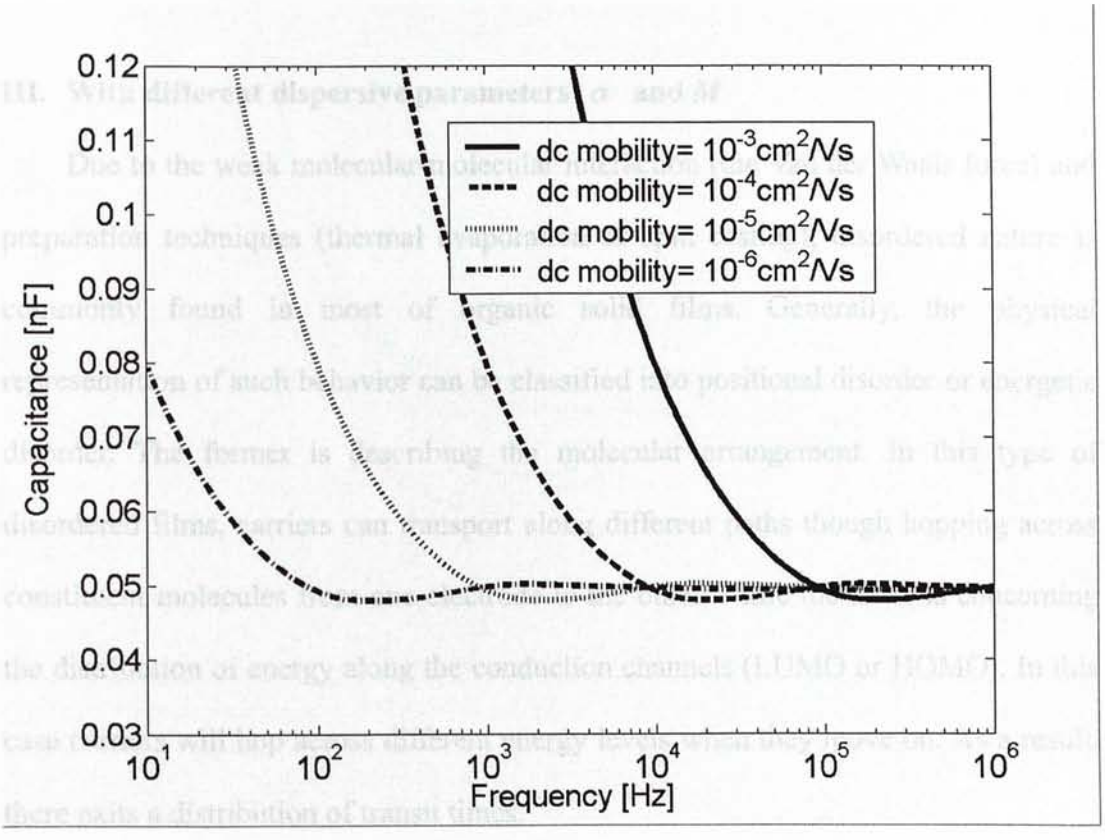

Figure 3.6. Frequency-dependent capacitance as a function of mobility.

Table 3.2. Simulation parameters for Fig. 3.6.

applied voltage V_{bias}	α	M	ε_r	thickness L	electrode area A
1 V	0.6	0.2	2.78	500 nm	10^{-2} cm^{-2}

In Fig. 3.6, the frequency-dependent capacitance is investigated with different carrier mobility. There is a minimum capacitance in each curve, and the curves are shifted towards higher frequencies with increasing the mobility. As discussed before, the capacitance minimum indicates the relaxation of the injected carriers inside the organic film. For an organic solid with a higher mobility, the time needed to achieve

a new equilibrium of space-charge distribution is shorter. Therefore for a solid with higher mobility, the minimum moves to higher frequency side.

III. With different dispersive parameters α and M

Due to the weak molecular-molecular interaction (the Van der Waals force) and preparation techniques (thermal evaporation or spin casting), disordered nature is commonly found in most of organic solid films. Generally, the physical representation of such behavior can be classified into positional disorder or energetic disorder. The former is describing the molecular arrangement. In this type of disordered films, carriers can transport along different paths though hopping across constituent molecules from one electrode to the other, while the latter is concerning the distribution of energy along the conduction channels (LUMO or HOMO). In this case carriers will hop across different energy levels when they move on. As a result, there exits a distribution of transit times.

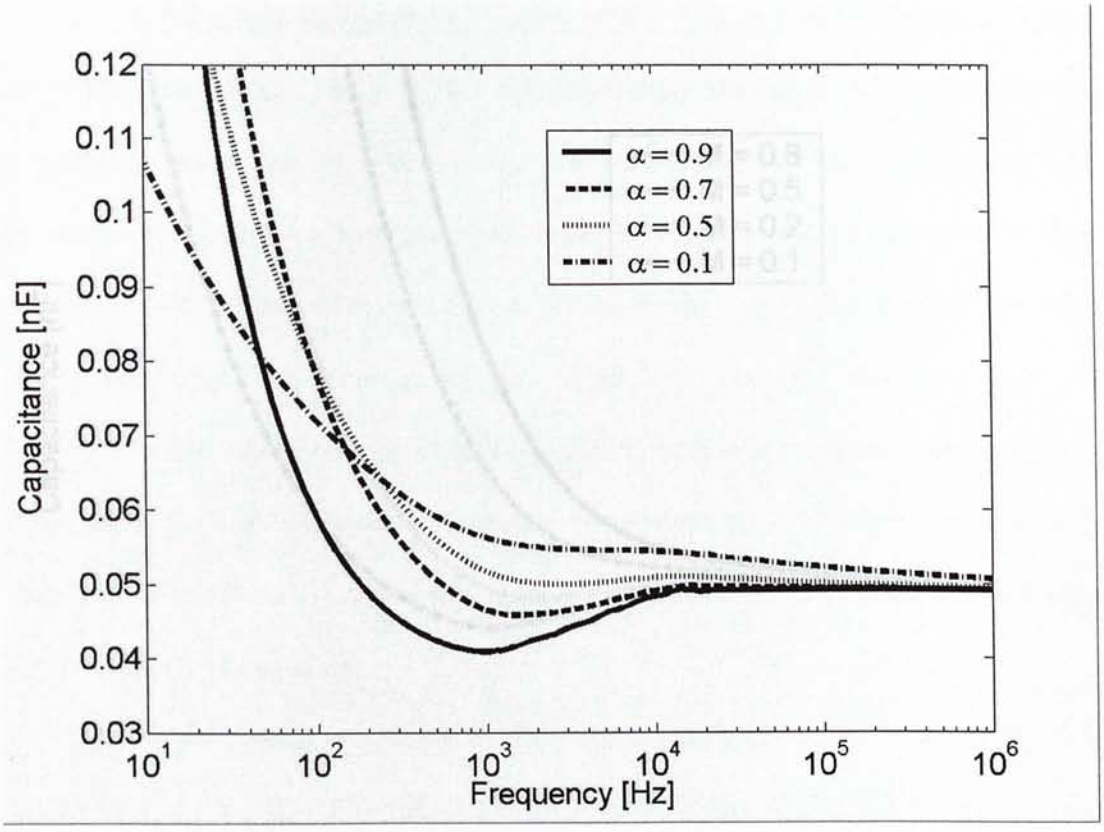

Figure 3.7. Frequency dependent capacitance as a function of dispersive parameter α.

Table 3.3. Simulation parameters for Fig. 3.7.

applied voltage V_{bias}	average mobility μ_{dc}	M	ε_r	thickness L	electrode area A
1 V	10^{-5} cm^{-2}/Vs	0.2	2.78	500 nm	10^{-2} cm^{-2}

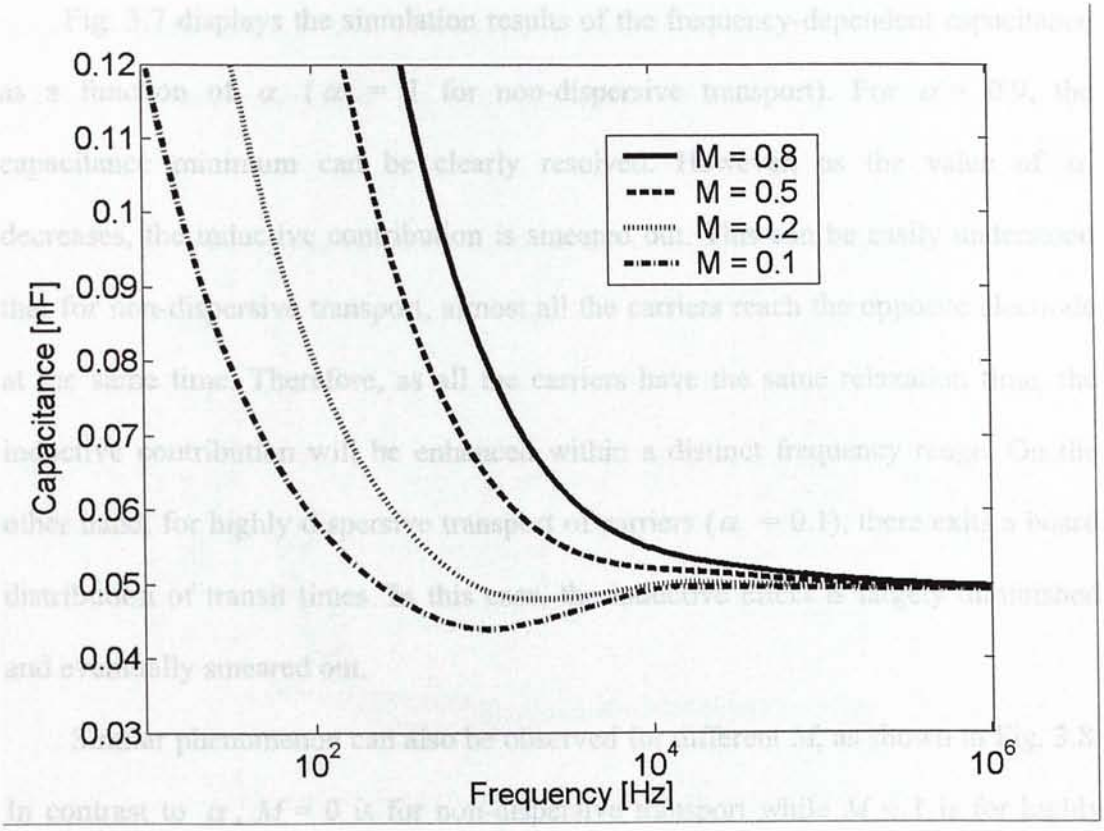

Figure 3.8. Frequency dependent capacitance as a function of dispersive parameter *M*.

Table 3.4. Simulation parameters for Fig. 3.8.

applied voltage V_{bias}	average mobility μ_{dc}	α	ε_r	thickness L	electrode area A
1 V	10^{-5} cm^2/Vs	0.6	2.78	500 nm	10^{-2} cm^{-2}

By considering the hopping mechanism along the conduction channel, an analytical expression of frequency dependent mobility $\tilde{\mu}(\Omega) = 1 + M(i\Omega)^{1-\alpha}$ was used [12]. In order to investigate the effect of dispersive behavior on the frequency-dependent capacitance, simulations were carried out on different value of α and M.

Fig. 3.7 displays the simulation results of the frequency-dependent capacitance as a function of α (α = 1 for non-dispersive transport). For α = 0.9, the capacitance minimum can be clearly resolved. However, as the value of α decreases, the inductive contribution is smeared out. This can be easily understood that for non-dispersive transport, almost all the carriers reach the opposite electrode at the same time. Therefore, as all the carriers have the same relaxation time, the inductive contribution will be enhanced within a distinct frequency range. On the other hand, for highly dispersive transport of carriers (α = 0.1), there exits a board distribution of transit times. In this case, the inductive effect is largely diminished and eventually smeared out.

Similar phenomenon can also be observed for different *M*, as shown in Fig. 3.8. In contrast to α, M = 0 is for non-dispersive transport while M = 1 is for highly dispersive transport. Besides, larger *M* will increase the carrier mobility. Therefore it will increase the capacitance as well.

From the simulation results of the carrier transport model described in Eq. 3.18, the frequency-dependent capacitance of organic solid film is quantitatively studied in terms of carrier mobility, applied dc voltage and dispersive parameters. It is demonstrated that there exists a minimum of capacitance in a distinct frequency region, which is responsible for the carrier relaxation. The carrier transit time and mobility can be extracted from this characteristic. The position of the minimum of capacitance is attributed to the time scale of carrier relaxation. It is clearly shown that the minimum of capacitance shifts to higher frequency by increasing the applied dc voltage or replacing a material with higher carrier mobility. For highly dispersive carrier transport, the width of the minimum is largely smeared out and diminished. In this case, the capacitance follows a monotonic increase from high to low frequency.

3.3.2 Experimental results of Au/CuPc/Au devices

3.3.2.1 Field dependent hole mobility in CuPc

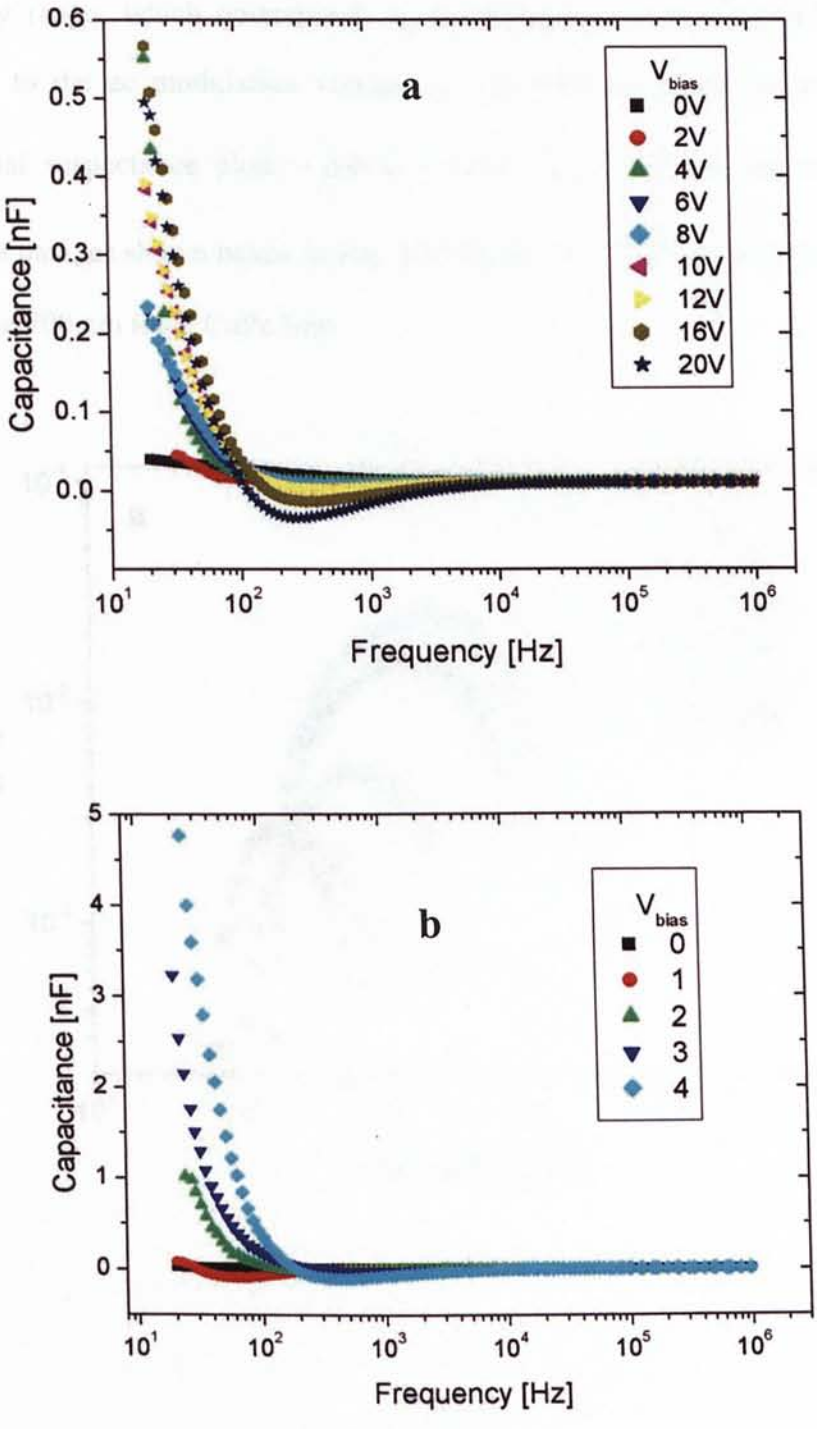

Figure 3.9. Frequency-dependent capacitance of Au/CuPc/Au devices as a function of applied bias. CuPc thickness is equal to 1400 nm for **(a),** and 700 nm for **(b)**.

Fig. 3.9 (a) and (b) show the frequency-dependent capacitance of two different CuPc films, 1400 nm thick and 700 nm thick, respectively. As predicted by the theoretical model [21-22], a small inductive effect can be observed in a distinct frequency range, which corresponds to the relaxation of the injected carriers in response to the ac modulation voltage v_{ac}. In order to attain the hole mobility, differential suspectance plots $-\Delta B(\omega) = -\omega(C - C_{geo})$ [23-24] are redrawn from the above data, as shown below in Fig. 3.10 (a) for the 1400 nm thick CuPc film, and (b) for the 700 nm thick CuPc film.

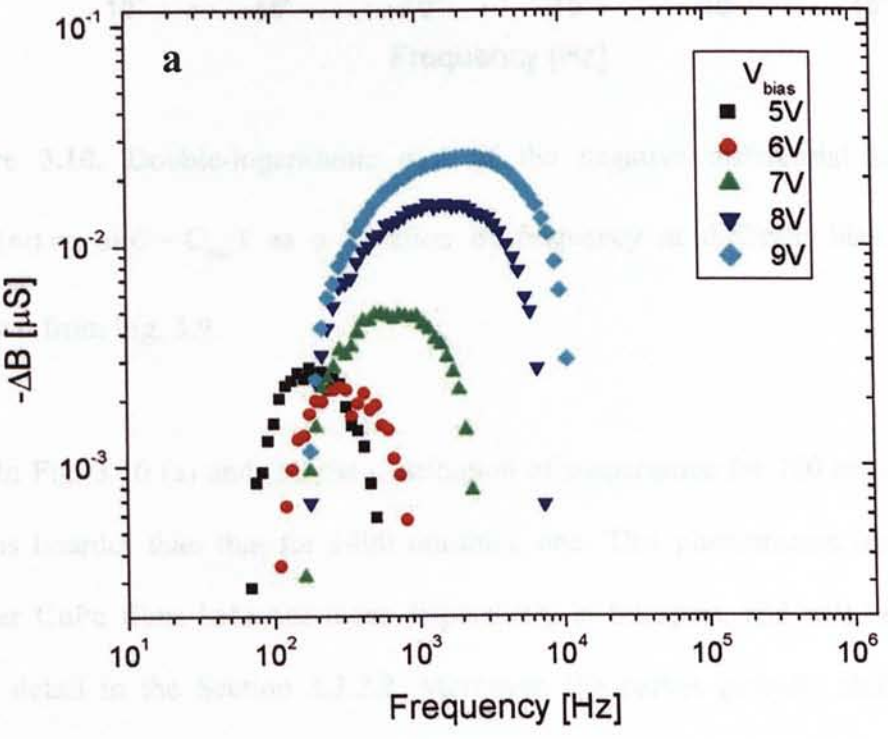

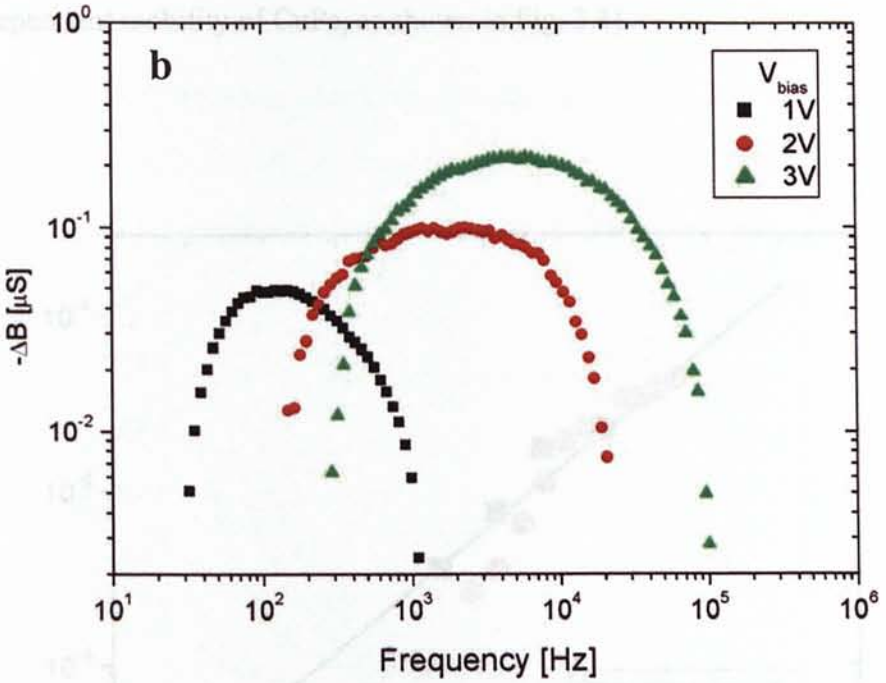

Figure 3.10. Double-logarithmic plot of the negative differential suspectance $-\Delta B(\omega) = -\omega(C - C_{geo})$ as a function of frequency at different bias. Date are redrawn from Fig. 3.9.

In Fig. 3.10 (a) and (b), the distribution of suspectance for 700 nm-thick CuPc film is boarder than that for 1400 nm-thick one. This phenomenon indicates that thinner CuPc films behavior more dispersively in transport, and will be discussed more detail in the Section 3.3.2.2. Moreover, the curves globally shift to higher frequency side as the bias increases, which corresponds to the decrease of transit time in a higher electric field. The relation between the applied field and carrier mobility in organic solids is generally described by the Poole-Frenkel field-dependent behavior $\mu_{dc} = \mu_0 \exp(\gamma\sqrt{E})$, where μ_0 is the zero field mobility, and γ is the field-dependent coefficient, E is the field strength. By selecting the

curve maxima from Figs. 3.10 (a) and (b), with $\tau = (2 \pm 0.5) \times \tau_t$, we now obtain the field-dependent mobility of CuPc, as shown in Fig. 3.11.

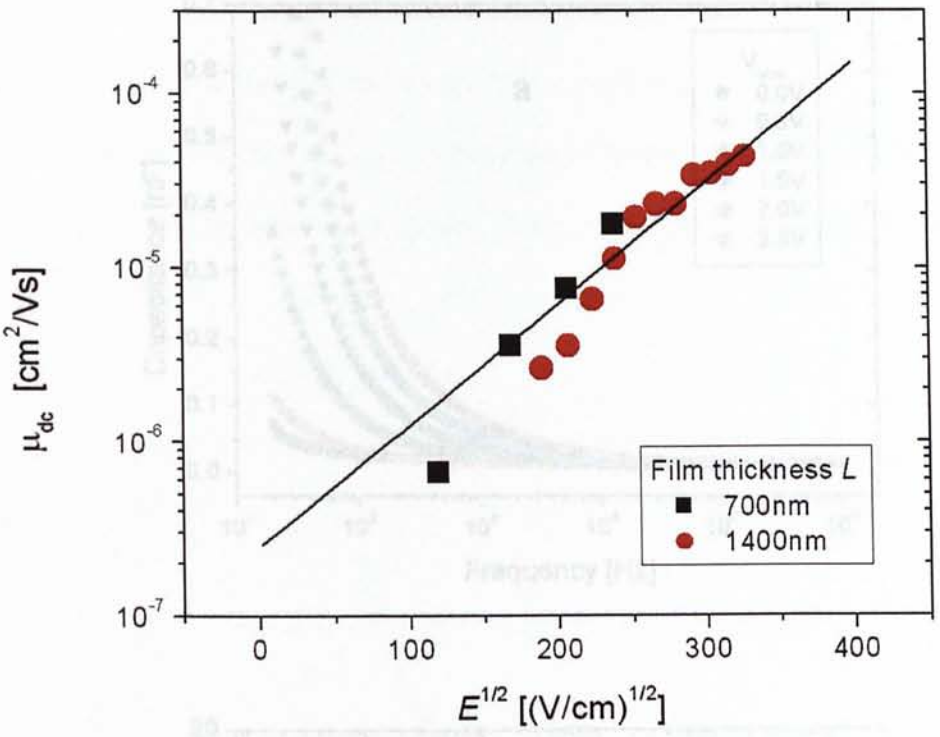

Figure 3.11. Field-dependent hole mobility of Au/CuPc/Au devices with different thickness L as a function of $E^{1/2}$. The solid line represents a fitting of μ_{dc} according to the Poole-Frenkel model.

By fitting the data to the Poole-Frenkel model $\mu_{dc} = \mu_0 \exp(\gamma\sqrt{E})$, now we attain $\mu_0 = (2 \pm 0.5) \times 10^{-7}$ cm^2/Vs and $\gamma = 0.017 \pm 0.001$(V/cm)$^{-1/2}$. Moreover, from the extracted hole mobility, the μ_{dc} independence of L proves that the dc mobility in fact represents the average attribution of carriers in the dispersive transport.

3.3.2.2 Thickness-dependent dispersive transport

In order to gain more insight in the thickness dependent dispersive transport behavior, thinner CuPc films were investigated.

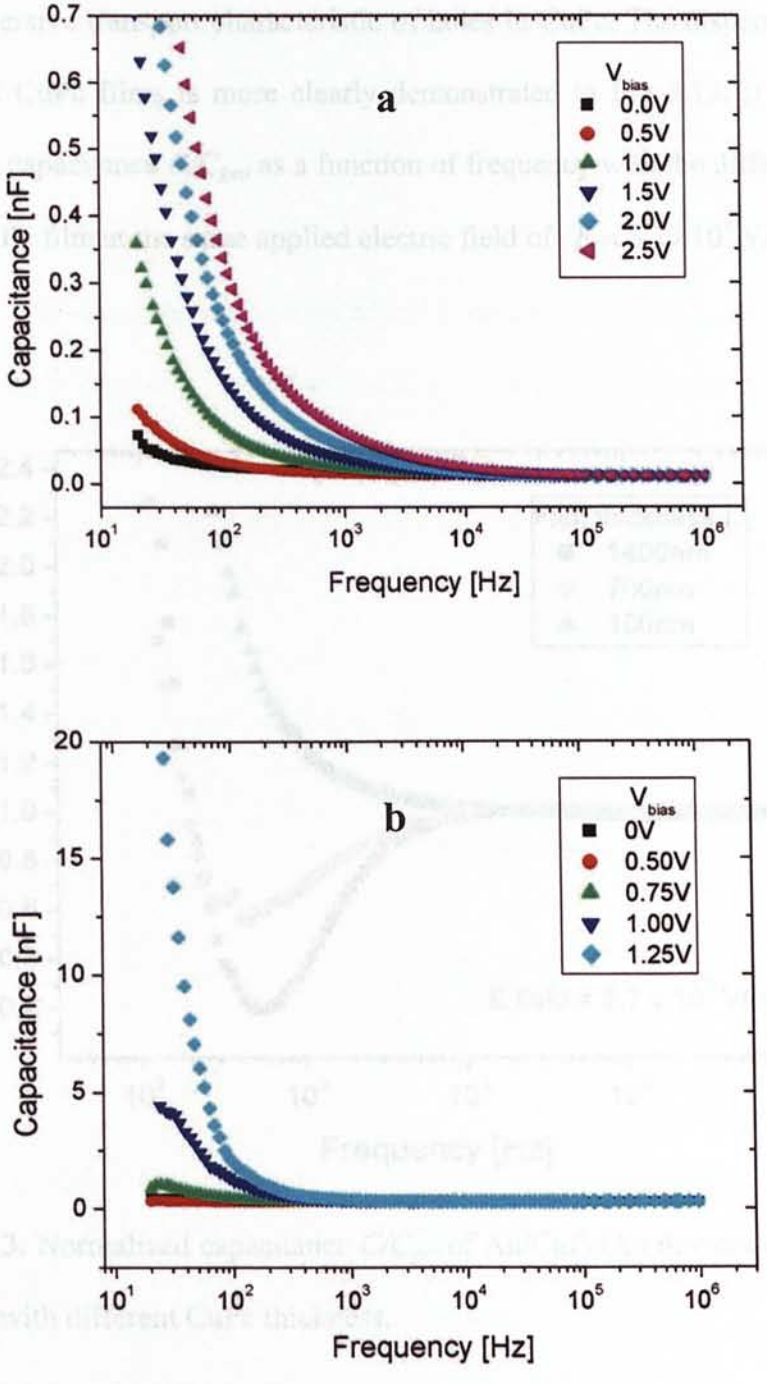

Figure 3.12. Capacitance of Au/CuPc/Au devices as a function of frequency at different biases for **(a)** 275 nm-thick CuPc film and **(b)** 100 nm–thick CuPc film.

Fig. 3.12 shows the frequency-dependent capacitance of (a) 275nm-thick CuPc film, and (b) 100nm-thick CuPc film in Au/CuPc/Au structure. In both cases, the capacitance shows a monotonic increase as the frequency varies from high frequency to low frequency. Therefore no inductive effect is observed. This results from the highly dispersive transport characteristic of holes in CuPc. The dispersivity of holes in different CuPc films is more clearly demonstrated in Fig 3.13. It manifests the normalized capacitance C/C_{geo} as a function of frequency with the different thickness L of the CuPc film at the same applied electric field of $E = 5.7 \times 10^4$ V/cm.

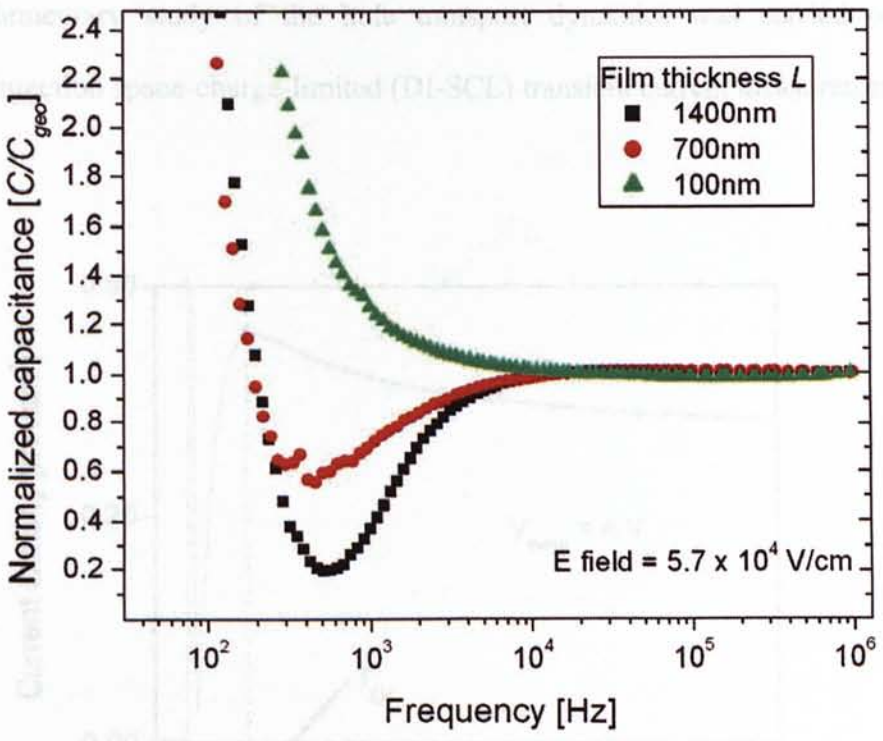

Figure 3.13. Normalized capacitance C/C_{geo} of Au/CuPc/Au devices as a function of frequency with different CuPc thickness.

It is seen that by increasing L the inductive contribution to the capacitance becomes more pronounced. This means that for thicker films the transit time τ_t distribution becomes narrowly defined. This demonstrates the relaxation of the dispersive transport towards equilibrium [21]. For short transit time, after carriers have only made a few hops, a broad distribution of charge carrier velocities appears. For a long transit time, i.e., after numerous hopping events, on average all carriers drift at the same velocity $v = \mu_{dc} E$.

3.3.3 Experimental results of Au/CuPc/Au devices by DI-SCL measurement

To comprehensively understand the results by admittance spectroscopy, a complementary study of the hole transport dynamics was carried out by the dark-injection space-charge-limited (DI-SCL) transient current measurement.

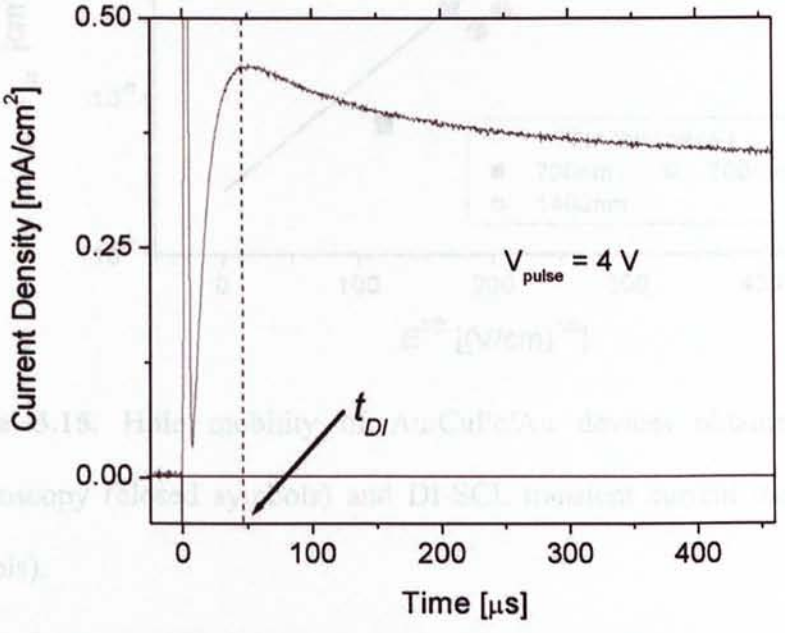

Figure 3.14. A typical DI-SCL transient current at $V_{pulse} = 4\,V$ of Au/CuPc/Au device with a 700 nm-thick CuPc film.

Fig. 3.14 shows a typical DI-SCL transient current of Au/CuPc(700nm)/Au device at $V_{pulse} = 4\,\mathrm{V}$ [1]. It provides the convincing evidence that the Ohmic injection contact is established at the Au and CuPc interface [25]. The position of the transient current maximum is related to the transit time of carrier by $t_{DI} = 0.786 \cdot \tau_t$. The measured mobility is plotted as a function of electric field strength. Then, according to $\mu_{dc} = \frac{L}{\tau_t E}$. Finally, the field-dependent mobility can be extracted in Fig. 3.15, with the measured values acquired by admittance spectroscopy. The mobility obtained by these two methods are in good agreement.

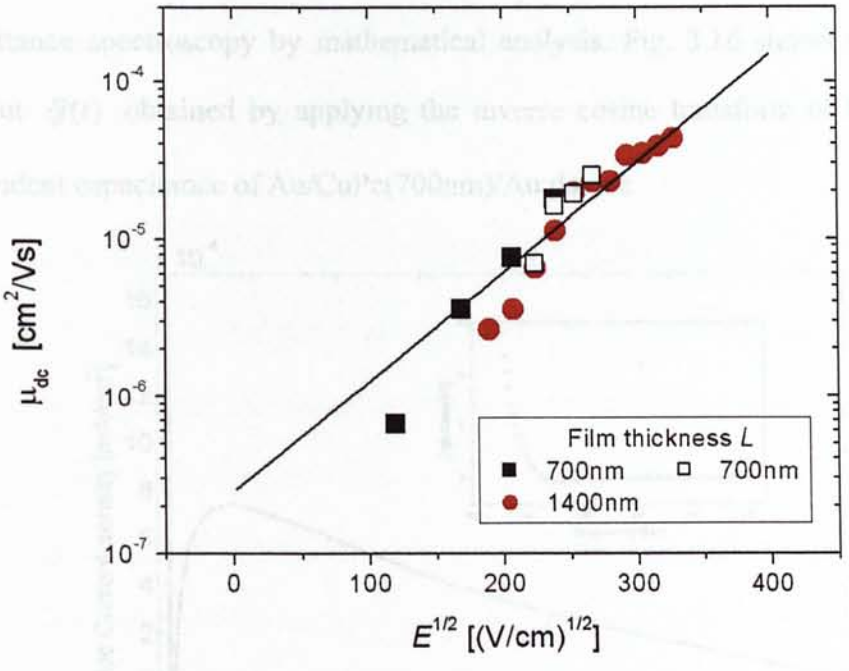

Figure 3.15. Hole mobility of Au/CuPc/Au devices obtained by admittance spectroscopy (closed symbols) and DI-SCL transient current measurements (open symbols).

In the case of small signal analysis, the time domain and frequency domain characteristics can be correlated by the Fourier Transformation[26], as shown in

Appendix B, i.e.

$$Y(\omega) = \frac{i\omega}{\Delta V}\int_0^\infty \delta I(t)e^{-i\omega t}dt \tag{3.20}$$

where $Y(\omega)$ is the admittance, ΔV is the applied voltage step and $\delta I(t)$ is the transient current. Therefore, we gain the capacitance in frequency domain as

$$C(\omega) = C_{geo} + \frac{1}{\Delta V}\int_0^\infty \delta j(t)\cos(\omega t)dt \tag{3.21}$$

with C_{geo} being the geometrical capacitance and $\delta j(t)$ being the relaxation current.

Although it is not a small signal application in DI-SCL transient current measurements, some general similarities are observable between DI-SCL method and admittance spectroscopy by mathematical analysis. Fig. 3.16 shows the relaxation current $\delta j(t)$ obtained by applying the inverse cosine transform of the frequency dependent capacitance of Au/CuPc(700nm)/Au device.

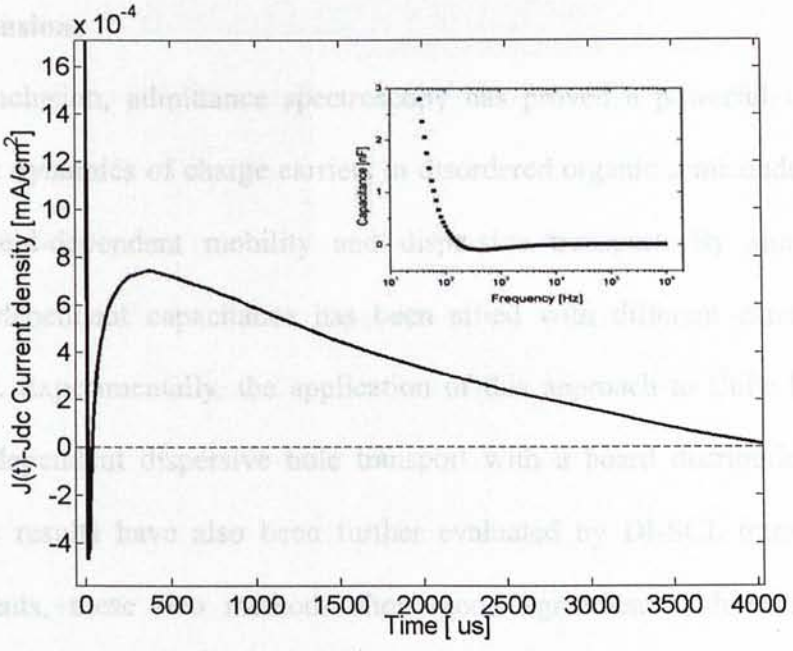

Figure 3.16. Relaxation current $\delta j(t)$ obtained by inverse cosine transformation of the frequency dependent capacitance of Au/CuPc(700nm)/Au device at 4V applied bias, that is shown by the inset.

By comparing the DI-SCL results shown in Fig. 3.14, the general attributes of the transformed relaxation current are very similar to those obtained experimentally. However, the mobility extracted from $\delta j(t)$ profile is about 7 and 6 times smaller than that obtained by admittance spectroscopy and DI-SCL, respectively. Nevertheless the consistence of the general characteristics is readily understood. At the very beginning of the transient current (<10 μs) in DI-SCL measurements, the rapid decrease corresponds to the small capacitance at high frequency (>100k Hz). After reaching the minimum, the current increases to a maximum value. Such an increase of current in time domain is equivalent to the appearance of inductive effect in a distinct frequency range in frequency domain. Finally, the transient current decreases gradually, which corresponds to the large capacitance value (the increasing *CR* constant) obtained at low frequency.

3.4 Conclusions

In conclusion, admittance spectroscopy has proved a powerful technique to explore the dynamics of charge carriers in disordered organic semiconductors in the case of field-dependent mobility and dispersive transport. By simulation, the frequency-dependent capacitance has been sifted with different carrier transport parameters. Experimentally, the application of this approach to CuPc has revealed thickness dependent dispersive hole transport with a board distribution of transit times. The results have also been further evaluated by DI-SCL transient current measurements, these two methods show good agreement with each other. By considering the small signal Fourier analysis, the correlation between frequency dependent capacitance and DI-SCL has been clearly demonstrated.

Reference

[1] M. A. Lambert, P. Mark, *Current Injection in Solids*, Academic Press, New York, NY (1970).

[2] W. D. Gill, J. Appl. Phys., **43,** 5033-5040 (1972).

[3] P. M. Borsenberger, D. S. Weiss, *Organic photoreceptors for imaging systems* (Dekker, New York, 1993), Chap. 8, p.181.

[4] M. Abkowitz, J. S. Facci, and J. Rehm., J. Appl. Phys. **83**, 2670 (1998).

[5] A. Ioannidis, J. S. Facci, M. A. Abkowitz, J. Appl. Phys. **84**, 1439 (1998).

[6] W. R. Salaneck and M. Lönglund, Polym. Adv. Technol. **9**, 419 (1998).

[7] V. –E. Choong, M. G. Mason, C. W. Tang, and Y. Gao, Appl. Phys. Lett. **72**, 2689 (1998).

[8] M. A. Abkowitz, H. A. Mizes, J. S. Facci, Appl. Phys. Lett. **66**, 1288 (1995)

[9] Y. Shen, K. Diest, M. H. Wong, B. R. Hsieh, D. H. Dunlap, and G. G. Malliaras, Phys. Rev. B **68**, 081204 (2003).

[10] P. R. Emtage, J. J. O'Dwyer, Phys. Rev. Lett. **16**, 356 (1966).

[11] J. C. Scott and G. G. malliaras, Chem. Phys. Lett. **299**, 155 (1999).

[12] J. C. Scott, Hopping conduction, private communication.

[13] D. Emin, Phys. Rev. Lett. **32**, 303 (1974).

[14] H. Scher and E. W. Montroll, Phys. Rev. B 12, 2455 (1977).

[15] H. Bässler, Phys. Status Solidi B **15**, 175 (1993)

[16] E. Gorham-Bergeron and E. Emin, Phys. Rev. B 12, 2455 (1975).

[17] H. Scher, M. Shlesinger and J. T. Bendler, Physics Today, p.26, January 1991.

[18] S. M. Sze, *Physics of Semiconductor Devices*, 2nd edition, John Wiley & Sons, 1981.

[19] M. van der Auweraer, F. C. De Schryverm, P. M. Borsenberger and H. Bässler,

Adv. Mater. 6, 199(1994).

[20] J. R. MacDonald, *Impedance Spectroscopy (*John Wiley and Sons, New York, 1987), Chap. 1, p. 2.

[21] H. C. F. Martens, J. N. Huiberts, and P. W. M. Blom, Appl. Phys. Lett. **77**, 1852(2000).

[22] S. Berleb and W. Brutting, Phys. Rev. Lett. **89**, 286601-1 (2002).

[23] H. C. F. Martens, J. N. Huiberts, and P. W. M. Blom, Appl. Phys. Lett. **77**, 1852(2000).

[24] P. W. M. Blom, H. C. F. Martens, J. N. Huiberts, Synth. Met. **121**, 1621 (2001).

[25] D. Poplavskyy, J. Nelson, and D. D. C. Bradley, Appl. Phys. Lett. **83**, 707(2003)

[26] M. Ershov, H. C. Liu, L. Li, M. Buchanan, Z. R. Wasilewski, and A. K. Jonscher, "Negative Capacitance Effect in Semiconductor Devices", IEEE Trans. Electron Devices, 45, p.2196 (1998).

[27] H. Bottger and V. V. Bryksin, *Hopping Conduction in Solids* (Akademie-Verlag, Berlin, 1985), Chap. 6, p.224.

Chapter 4

NEGATIVE CAPACITANCE IN Au/CuPc/Au DEVICES

Abstract

Negative capacitance (NC) observed in Au/copper phthalocyannie(CuPc)/Au devices is comprehensively investigated. When a high dc bias is applied to the device, a large NC effect is found in a frequency range below 1 kHz by admittance spectroscopy. This phenomenon is concurrently studied by dark injection space-charge-limited (DI-SCL) transient current measurements, and conventional current-voltage (I-V) measurements. By combining the current-voltage (I-V) and capacitance-voltage (C-V) characteristics (<100 Hz), the negative capacitance is found within the trap filling region when the ac modulation frequency is less than 100Hz. A mechanism based on the trap filling process is proposed to explain the observed phenomenon.

4.1 Introduction to negative capacitance in different material systems

In most of organic semiconductor applications, carrier injection and transport play a very important role on device performance. Understanding the underlying mechanisms of the related processes is necessary to find clues for improving device performance and exploring novel applications. Capacitance characteristics provide a powerful spectroscopy method for nondestructive investigation of semiconductor devices and evaluation of their structural and electrical parameters.

Although negative capacitance (NC), or in another team inductive effect, has been report in different material systems [1], such as GaAs multiple quantum well (MOW) infrared photodetectors[2] , porous TiO_2[3], metallic nanoparticles embedded in dielectric matrix [4], and polymer light-emitting diode [5], the microscopic mechanisms behind NC are varied and should be determined by carrier transport properties and energy-band diagram of the respective materials. Generally, the correct interpretation of NC is based on the analysis of the time-domain transient current in response to a voltage pulse or step [6]. In this case the time-derivative transient current has a positive value, which corresponding to the frequency range where the NC occurs.

In this Chapter, a series of experiments are described that the NC effect was observed in Au/copper phthalocyannie(CuPc)/Au devices. A complementary study by dark injection space-charge-limited transient current measurements (DI-SCLC) of this phenomenon will also be presented. In order to attain a deeper insight of the underlying mechanisms, a combination of the current-voltage (*J-V*) and capacitance-voltage (*C-V*) characteristics will be discussed with a proposed mechanism based on the trap filling process.

4.2 Experimental

4.2.1 Experimental scheme

The *J-V* and impedance measurements were preformed by Hewlett Packard 4145B semiconductor parameter analyzer, and 4284A impedance analyzer respectively. The sweeping frequency of the impedance analyzer was in a range from 20 Hz to 1 MHz. During the measurements different dc voltages v_{dc} were chosen to superimpose with an ac modulation signal v_{ac}, and the capacitance value of the devices was found to be independent of v_{ac}. For each application of dc voltage, a pause in 30 seconds was used to stabilize the devices before acquiring the data. For the dark injection space-charge-limited (DI-SCL) transient current measurements, a voltage pulse was applied to the Au electrodes and the resulting transient current measured by LeCroy LT264, digital oscilloscope. In order to ensure the injected carriers are fully relaxed before each pulse, duty cycle (pulse length / repetition unit) less then 1% was chosen. All the measurements were performed at room temperature in air, and there was no visible evidence of the sample degradation during the measurements.

4.2.2 Sample preparation

The device structure under investigation consists of a single layer of copper phthalocyannie (CuPc) thin film was sandwiched by two Au electrodes on a quartz substrate. High purity of CuPc was purchased from Zencatec Co. without further purification. Au was procured from Aldrich Co. at the highest purity available. The Au electrodes and CuPc thin films were thermally evaporated though shadow masks inside a vacuum chamber at a base pressure of $2\sim3\times10^{-6}$ Torr. In order to ensure the film uniformity, the distance between the source and sample holder was separated by at least 20 cm and the evaporation rate was controlled at 0.3-0.5 Å/s.

4.3 Data analysis and discussions

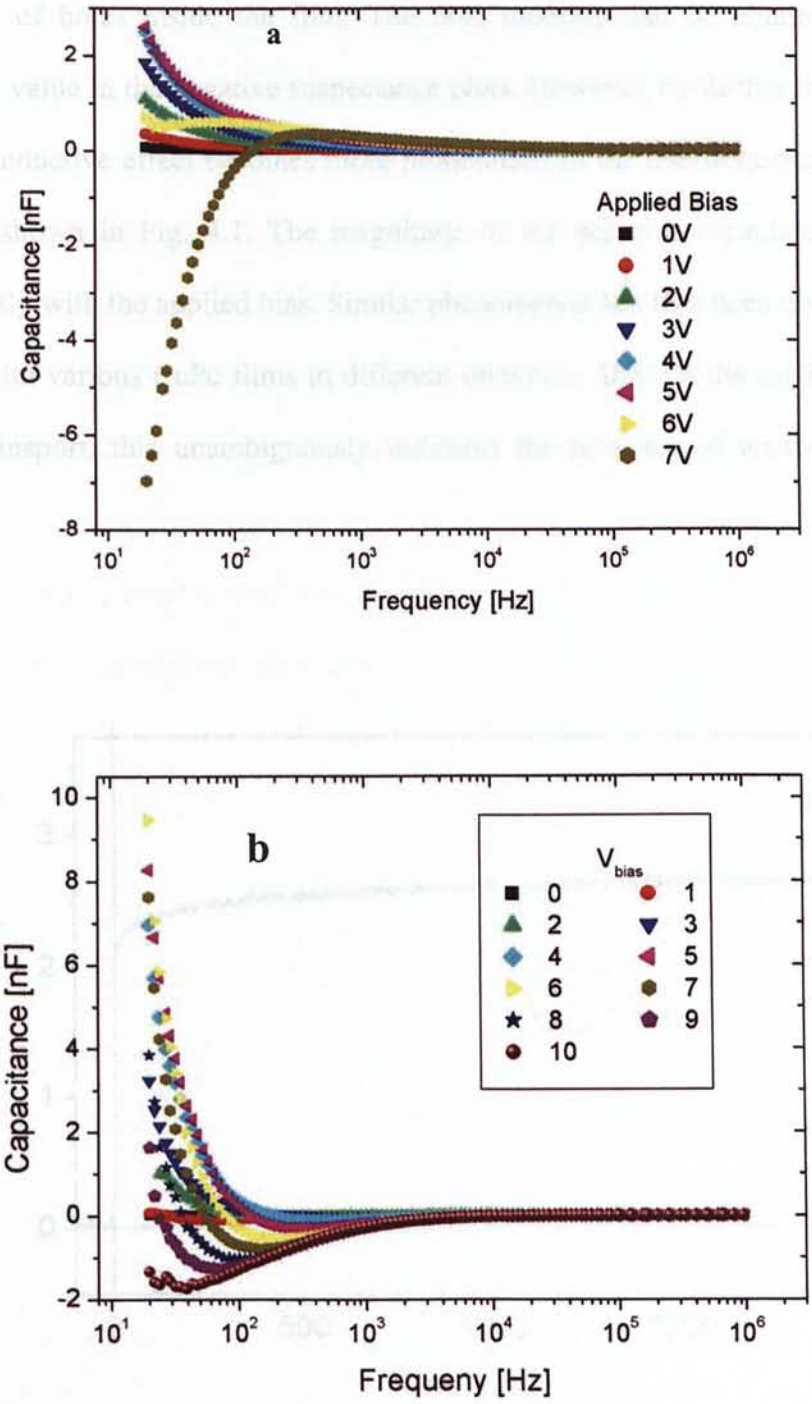

Figure 4.1. Frequency-dependent capacitance as a function of applied bias Au/CuPc/Au devices with a CuPc film in thickness of **(a)** 275 nm **(b)** 700 nm.

As discussed previously in Chapter 3, in the low bias region, small but distinguishable inductive effect is seen, which presumably corresponds to the relaxation of holes inside the film. The hole mobility can be obtained from the maximum value in the negative suspectance plots. However, by further increasing the bias, the inductive effect becomes more pronounced in the low frequency region (<1 kHz), as shown in Fig. 4.1. The magnitude of the negative capacitance increases significantly with the applied bias. Similar phenomenon has also been observed in the devices with various CuPc films in different thickness. Besides the carrier relaxation during transport, this unambiguously indicates the presence of another relaxation process.

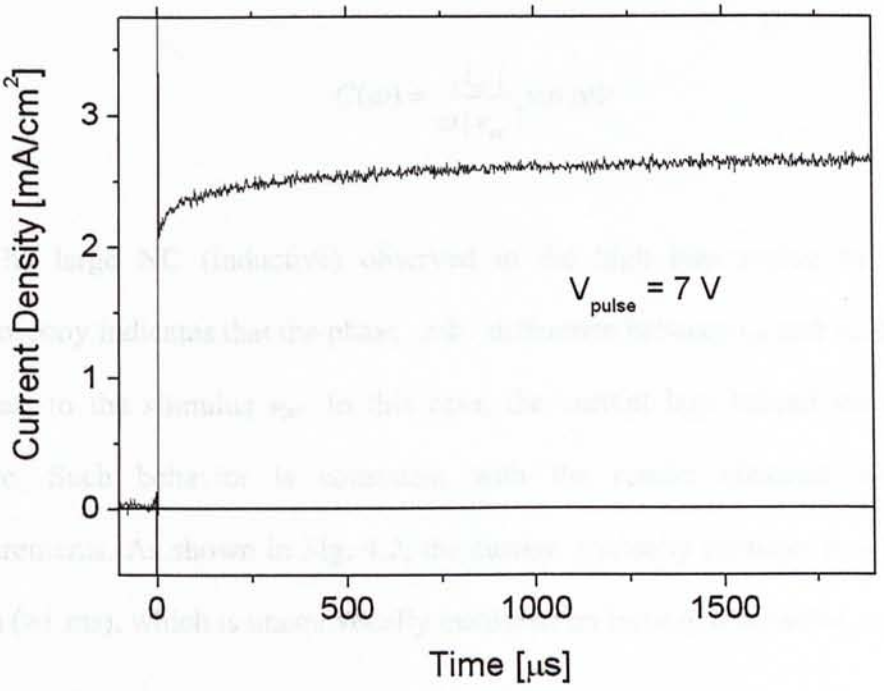

Figure 4.2. The dark injection space-charge-limited transient current (DI-SCLC) profile of Au/CuPc(700 nm)/Au in response to a voltage pulse of 7 V.

A complementary study of this phenomenon was carried out by the DI-SCLC measurements, as shown in Fig. 4.2. The same sample of device of Au/CuPc/Au with a 700 nm-thick CuPc film in the admittance spectroscopic was selected. In the low bias (<6V) region, as discussed previously in Chapter 3, a typical DI-SCLC profile commonly appears. The transit time can be determined by the location of the maximum transient current. However, by increasing the applied voltage pulse, the expected maximum gradually disappears, and the current slowly saturates in a longer time frame. The transition voltages from capacitive to inductive characteristics obtained by admittance spectroscopy and DI-SCLC measurements are in good consistence with each other.

Capacitance is defined as the magnitude and phase differences between the ac current i_{ac} and ac modulation voltage v_{ac}. i.e.

$$C(\omega) = \frac{|i_{ac}|}{\omega |v_{ac}|} \sin \Delta\Phi \tag{4.1}$$

The large NC (inductive) observed in the high bias region by admittance spectroscopy indicates that the phase $\Delta\Phi$ difference between i_{ac} and v_{ac} decreases in response to the stimulus v_{ac}. In this case, the current lags behind the modulation voltage. Such behavior is consistent with the results obtained by DI-SCLC measurements. As shown in Fig. 4.2, the current gradually saturates in a longer time region (>1 ms), which is unequivocally manifests an inductive behavior.

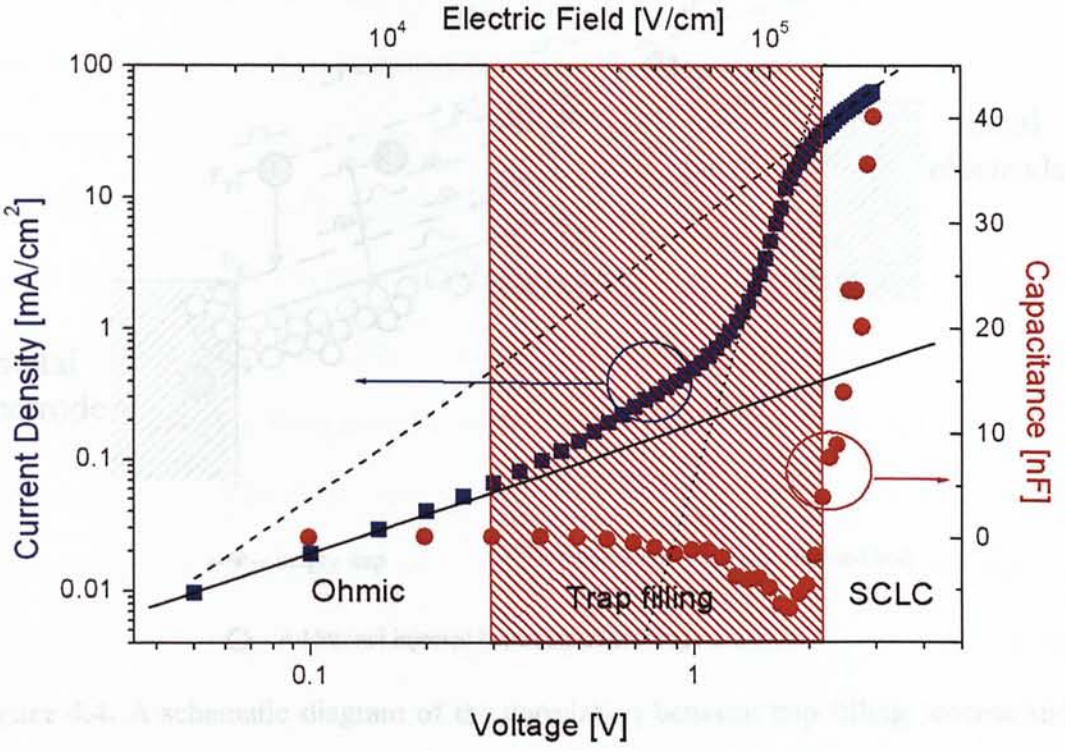

Figure 4.3. The *J-V* and *C-V* characteristics of a Au/CuPc/Au device with a 165 nm-thick CuPc film.

In order to acquire a deeper insight into the origins of the strong inductive effect at low frequency, *C-V* and *J-V* measurements were concurrently carried out for comparison. Fig. 4.3 shows the *C-V* and *J-V* characteristics of a Au/CuPc/Au device with a 165 nm-thick CuPc film, and the frequency used was 20 Hz in *C-V* measurements. The *J-V* characteristics can be clearly divided into three different regions, Ohmic, traps filling, and pure SCLC regions. In the Ohmic region, the value of capacitance is positive and slight increases with the bias. However, once it enters the trap filling region, the capacitance value largely drops to negative and finally reaches a minimum. By further increasing the bias, it increases again and goes to positive in the pure SCLC region.

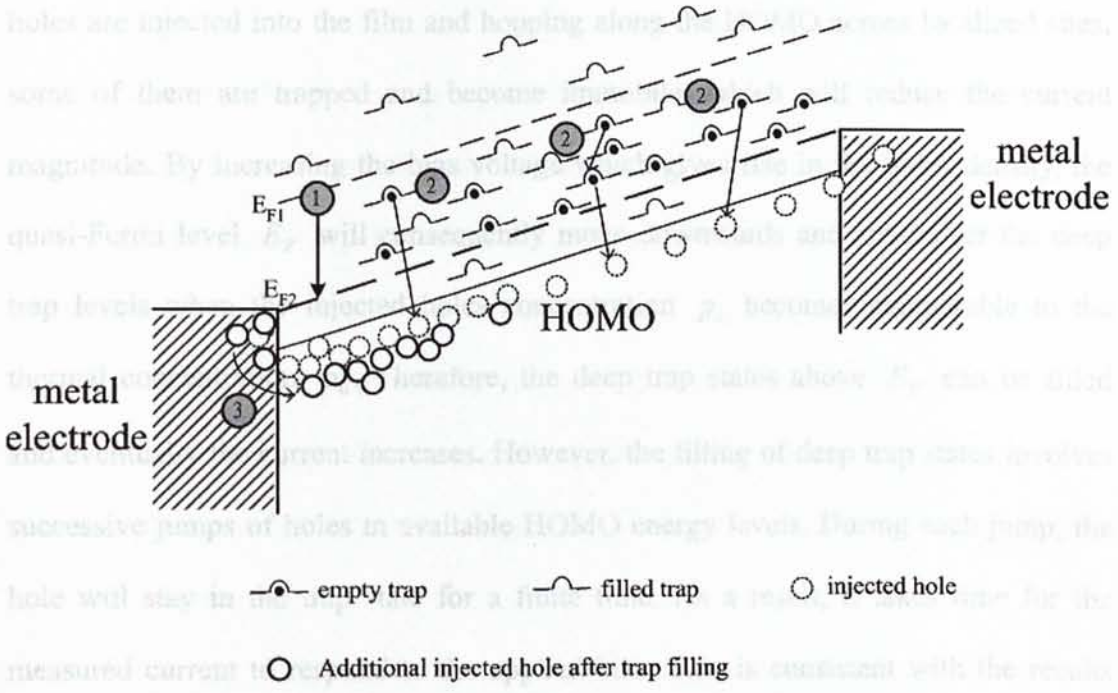

Figure 4.4. A schematic diagram of the correlation between trap filling process and negative capacitance.(1) Hole density increased by increasing of bias and eventually moves the Fermi level, E_F downward. (2) More deep traps filled by holes. (3) As the number of traps decreases, the number of injected holes in HOMO increases, and therefore the current increases. As a result, the time-consumed trap filling process induces an additional increased current which lags behind the ac modulation voltage v_{ac}. This effect results in the negative capacitance.

Based on the above results, it is suggested that the negative capacitance appeared in Au/CuPc/Au devices in the high bias and low frequency conditions is owing to the slow trap filling process. Due to the disorder nature of organic solid films, the edges of conduction channel (HOMO or LUMO) are not well defined, and the density of states of the channel always has a Gaussian distribution [6]. Therefore, an exponential distribution of trap states with characteristic energy E_t between 0.1eV and 0.4eV away from the conduction channels are commonly found in most of organic solids [7][8]. Moreover, the Fermi level of CuPc is about 0.7eV above its HOMO [9]. Once the

holes are injected into the film and hopping along the HOMO across localized sites, some of them are trapped and become immobile, which will reduce the current magnitude. By increasing the bias voltage which gives rise in the holes density, the quasi-Fermi level E_F will consequently move downwards and cross over the deep trap levels when the injected holes concentration p_i becomes comparable to the thermal concentration p_0. Therefore, the deep trap states above E_F can be filled and eventually the current increases. However, the filling of deep trap states involves successive jumps of holes in available HOMO energy levels. During each jump, the hole will stay in the trap state for a finite time. As a result, it takes time for the measured current to respond to the applied bias. This is consistent with the results measured by the DI-SCLC measurements in the high bias region, as shown in Fig. 4.2. In the admittance spectroscopic measurements, the slow trap filling process introduces an increased current which lags behind the ac modulation voltage v_{ac}. Therefore the filling process is responsible for the large negative capacitance (or equivalently inductive effect) in the low frequency region. The correlation between negative capacitance and trap filling process is schematically proposed in Fig. 4.4.

Conclusions

A large negative capacitance (NC) (or equivalently strong inductive effect) is unequivocally observed by admittance spectroscopy at frequency lower than 1k Hz. This is further corroborated by dark injection space-charge-limited transient current measurements. By combining *C-V* and *J-V* characteristics of Au/CuPc/ Au devices, it is found that the NC occurs when the applied bias is high enough to enter the trap filling region. Owing to the slow trap filling process, the lag of the altered current in response to v_{ac} is deemed to be responsible for the large negative capacitance in the low frequency region.

Reference

[1] F. Lemmi and N. M. Johnson, Appl. Phys. Lett. **74**, 251 (1999).

[2] M. Ershov, H. C. Liu, L. Li, M. Buchanan, Z. R. Wasilewski, and V. Ryzhii, Appl. Phys. Lett. **70**, 1828 (1997).

[3] V. Kytin, Th. Dittrich, and F. Koch, Appl. Phys. Lett., **79**, 109 (2001).

[4] G. B. Parravicini, A. Stella, M. C. Ungureanu, and R. Kofman, Appl. Phys. Lett. **85**, 303 (2004).

[5] H. C. F. Martens, J. N. Huiberts, and P. W. M. Blom, Appl. Phys. Lett. **77**, 1852(2000).

[6] M. Ershov, H. C. Liu, L. Li, M. Buchanan, Z. R. Wasilewski, and A. K. Jonscher, "Negative Capacitance Effect in Semiconductor Devices", IEEE Trans. Electron Devices, 45, p.2196 (1998).

[7] M. Kiy, P. Losio, I. Biaggio, M. Keohler, A. Tapponnier, and P. Gunter, Appl. Phys. Lett., **80**, 1198 (2002).

[8] V. Kumar, S. C. Jain, A. K. Kapoor, J. Poortmans, and R. Mertens, J. Appl. Phys. **94**, 1283 (2003).

[9] Li Yan, N. J. Watkins, S. Zorba, Yongli Gao, and C. W. Tang, Appl. Phys. Lett. **79**, 4148 (2001).

Chapter 5

Hole Transport in Copper Phthalocyannine Under Various Ambient Conditions

Abstract

This chapter begins with the introduction to current development of organic sensors. Some proposed physical mechanisms will be highlighted. Experimentally, the effect of various ambient conditions (vacuum, oxygen, nitrogen, and relative humidity) on organic thin films will be demonstrated by J-V measurements. It is then followed by the investigation of transient current under various relative humidity (RH) levels. In order to understand more clearly the mechanisms, admittance spectroscopy is employed to monitor the carrier mobility for each condition.

5.1 Introduction

5.1.1 Current development of organic sensors.

It is widely known that most of organic materials are highly sensitive to the environment. In the negative side, this not only creates numerous difficulties in material characterization, but also obstructs organic devices in normal operation and accelerates their degradation. However, in the positive side, this sheds light in the field of sensor applications.

Gas and humidity sensing properties of some organic semiconductors have been a popular topic for years. Generally, the conductivity of organic solid films can be altered by oxidizing gases (Cl_2, O_2, NO, NO_2) or humidity. Different kinds of molecular structures have been designed to enhance the sensitivity. Conventionally the inter-digital transducers (IDTs) , as shown in Fig. 5.1, have been widely used. Output signals cab be multiplied by increasing the number of sensing channels. Recently, organic thin film transistors (OTFTs), as shown in Fig. 5.2, have been proposed as multi-parametric gas and humidity sensors [1-4]. Several device parameters of an OTFT, such as the saturation current, the off-current, the voltage threshold, and the subthreshold slope, are found to alter correspondingly in response to the variations of gases, volatile organic compounds, and humidity.

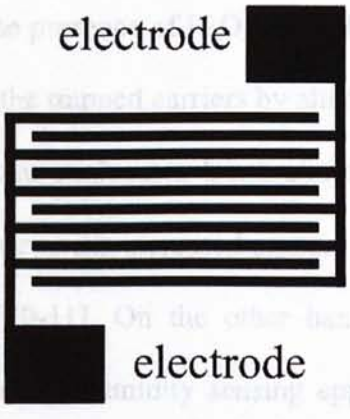

Figure 5.1. Inter-Digital Transducer.

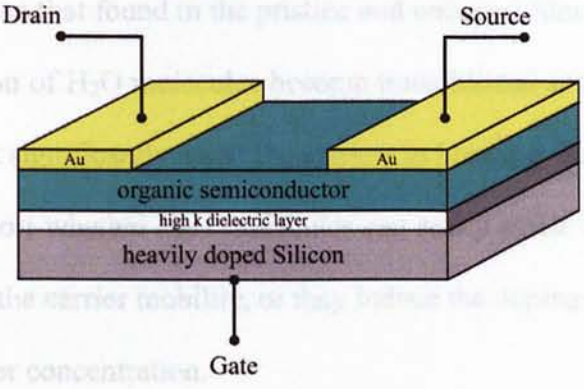

Figure 5.2. Organic field effect transistor.

5.1.2 Underlying mechanisms in sensing applications.

The underlying mechanisms in most of gas sensing applications are attributed to the doping effect from the interactions among organic and gas molecules [5-9]. For example, oxidation process will likely take place among oxidizing gases (O_2, O_3, NO, NO_2, etc.) and organic semiconductors. The oxidation usually results in a p-type doping effect.

Interestingly, the humidity effect largely depends on materials and structures. For example, it is found that in a hydrophobic pentacene OFET, the drain current I_d decreases with increasing the humidity a fixed gate voltage [1]. The mechanism behind this phenomenon is the presence of H_2O molecules which diffuse into the gain boundaries and interact with the trapped carriers by altering the electric field there. As a result, the presence of polar molecules bring about the reduced rate of charge transport in organic solids, due to the increased amount of energetic disorder through charge-dipolar interactions [10-11]. On the other hand, some hydrophilic organic materials have been employed in humidity sensing applications [12]. Especially, in phthalocyanines (Pcs), it is found that a large number of H_2O molecules are readily

incorporated with the Pc film and increase its conductivity to a few orders of magnitude higher than that found in the pristine and undoped film [13]. It is suggested that a sizable fraction of H_2O molecules become immobilized at the shallow trapping sites in the bulk that significantly assist the carriers in hopping. However, it falls short of evidence to support whether H_2O molecules can really assist carrier transport and eventually increase the carrier mobility, or they induce the doping effect that results in the increase in carrier concentration.

In this chapter, a series of experiments will be described to investigate the hole dynamics in Au/CuPc/Au devices under various ambient conditions. The *J-V* and transient current characteristics will be demonstrated to show the static response of the devices. In order to gain a deeper insight into the effects on carrier dynamics, the carrier mobility will be deduced by admittance spectroscopy.

5.2 Experimental

5.2.1 Experimental scheme

The *J-V* and transient current measurements were preformed by Hewlett Packard 4145B semiconductor parameter analyzer. Admittance spectroscopy was carried by Hewlett Packard 4284A impedance analyzer. The devices just after preparation were installed in the probe station with adjustable ambient conditions, as shown in Fig. 5.3.

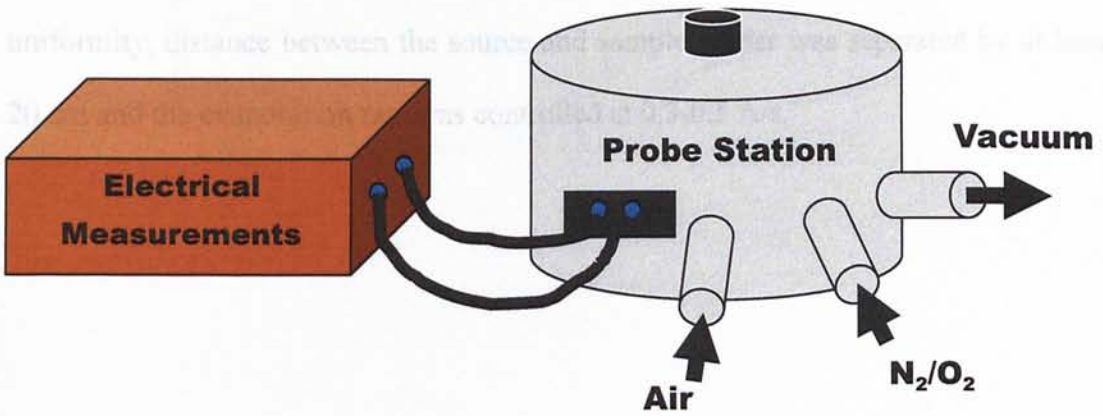

Figure 5.3. Experimental setup for electrical measurements in various ambient conditions.

For each measurement, in order to stabilize the devices, they were kept under the selected condition for 30 minutes before carrying the *J-V* and admittance measurements. After the measurement, another 30 minutes were used to restore the devices to their initiate situations by remaining them in vacuum with a base pressure below 1 Torr. In gas sensing experiments, pure dry nitrogen or oxygen gases were purged into the probe station with a flux at 1 atmospheric pressure. In humidity sensing experiments, the humidity was controlled by venting certain amount of air into the chamber, which was monitored by an electronic humidity senor with 10 to 15 seconds response time.

5.2.2 Sample preparation

The device structure under investigation consists of a single layer of copper phthalocyannie (CuPc) thin film sandwiched by two Au electrodes on a quartz substrate. High purity of CuPc has been purchased from Zencatec Co without further purification. Au was procured from Aldrich at the highest purity available. The Au electrodes and CuPc thin films were thermally evaporated though shadow masks in a vacuum chamber at a base pressure of $2\text{-}3\times 10^{-6}$ Torr. In order to ensure the film uniformity, distance between the source and sample holder was separated by at least 20 cm and the evaporation rate was controlled at 0.3-0.5 Å/s.

5.3 Data analysis and discussions

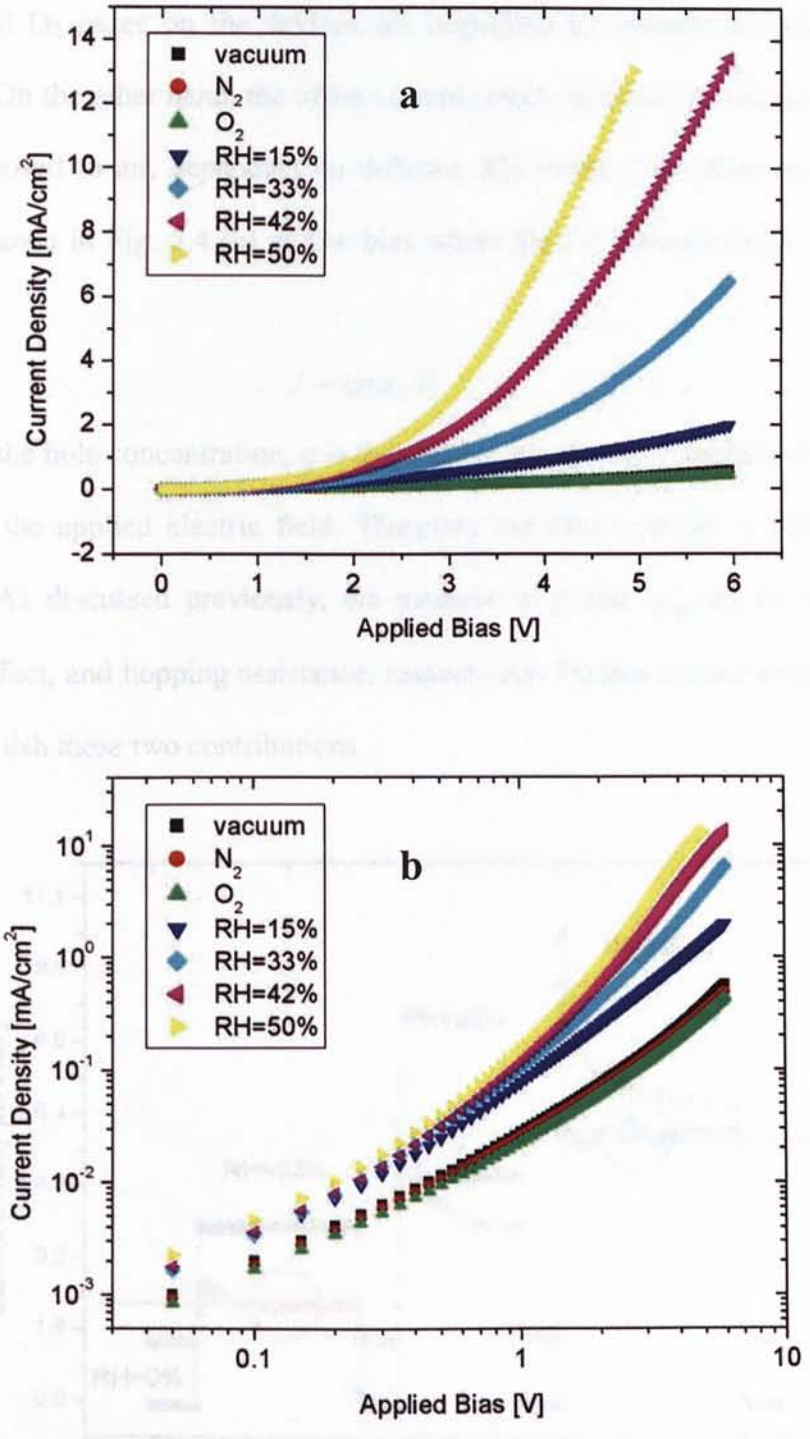

Figure 5.4. The linear (a) and logarithm (b) plots of the *J-V* characteristics of Au/CuPc(500 nm)/Au device in various conditions; a low vacuum (1 Torr), N_2 and O_2 atmospheres, and air with different RH levels.

Fig. 5.4 shows the *J-V* characteristics of Au/CuPc(500 nm)/Au device in a low vacuum (1 Torr), N_2 and O_2 atmospheres, and air with different RH levels. The effects of N_2 and O_2 gases on the devices are negligible in comparison with the *J-V* in vacuum. On the other hand, the offset current largely increases in the low boas region when exposed to air, dependent on different RH levels. The offset current is more clearly shown in Fig. 5.4 (b) at low bias where the *J-V* characteristics obeys Ohm's law:

$$J = qp\mu_{dc}E \tag{5.1}$$

with p is the hole concentration, q is the electron charge, μ_{dc} is the average mobility and E is the applied electric field. Therefore the offset current is related to $p\mu_{dc}$ product. As discussed previously, the increase in p and μ_{dc} can be regarded as a doping effect, and hopping assistance, respectively. Further studies should be carried to distinguish these two contributions.

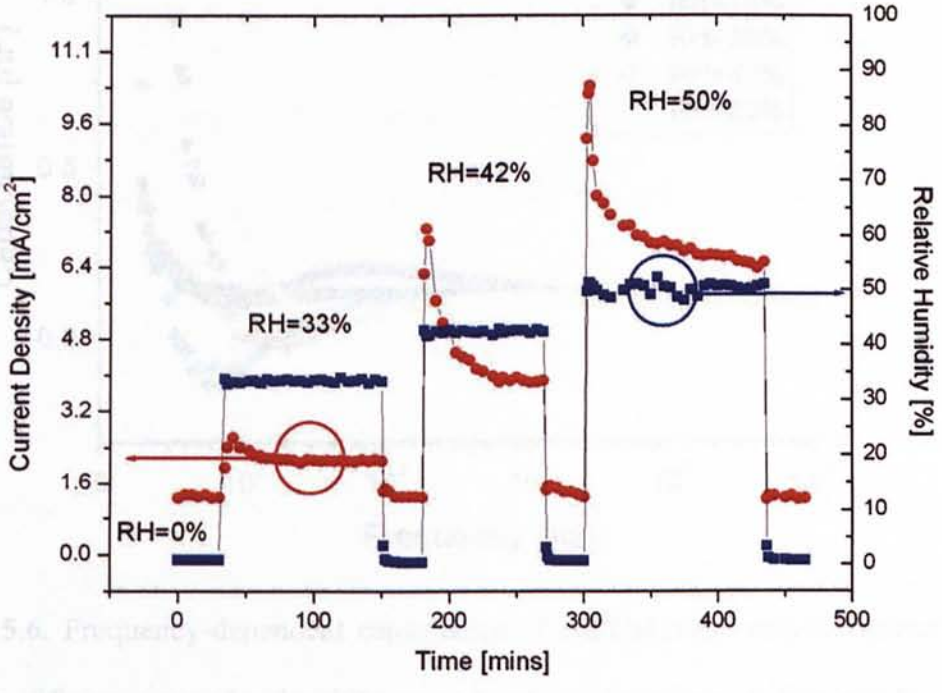

Figure 5.5. The current density in time domain measurement at 4V applied bias at different RH levels.

To further explore the sensing capability of Au/CuPc/Au devices, the current density of the device in time-domain was measured at a fixed bias of 4V. Fig. 5.5 displays the transient response of the device at 4V applied bias at different RH levels. The devices demonstrate a very good reproducibility in the *J-V* characteristics. The current density rapidly reaches a maximum in 3 to 5 minutes and gradually saturates. The overshoot in the transient current indicates that the film was highly absorbing in H_2O molecules [13]. Due to the concentration gradient, once the device is exposed to H_2O molecules, a large number of the molecules are absorbed, and it gradually reaches an equilibrium condition.

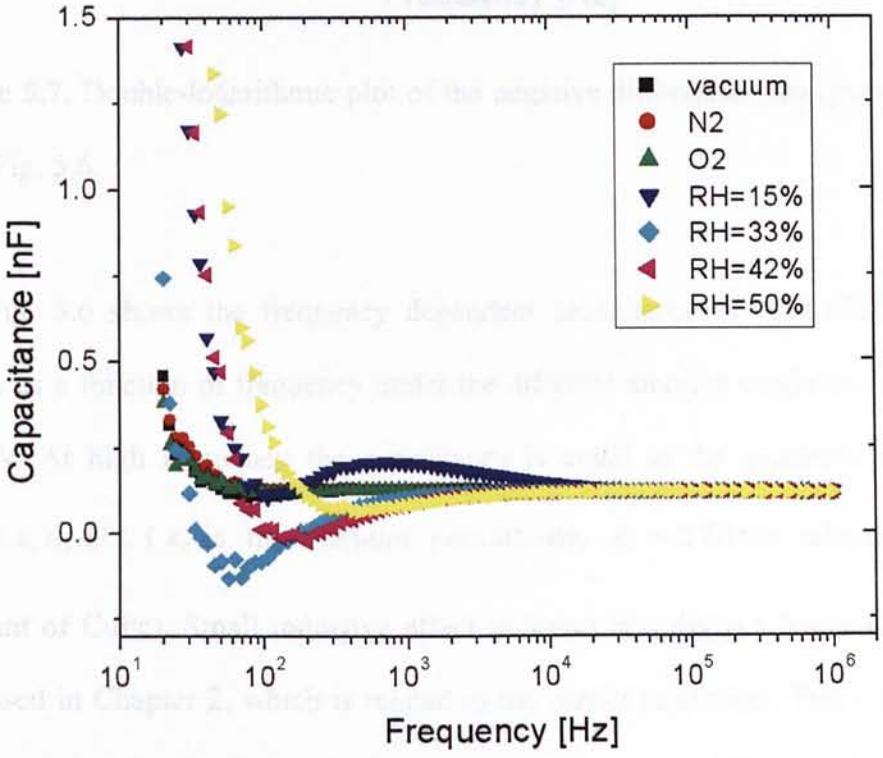

Figure 5.6. Frequency-dependent capacitance of Au/CuPc(500 nm)/Au device as a function of frequency under the different ambient conditions at a dc bias of 2 V.

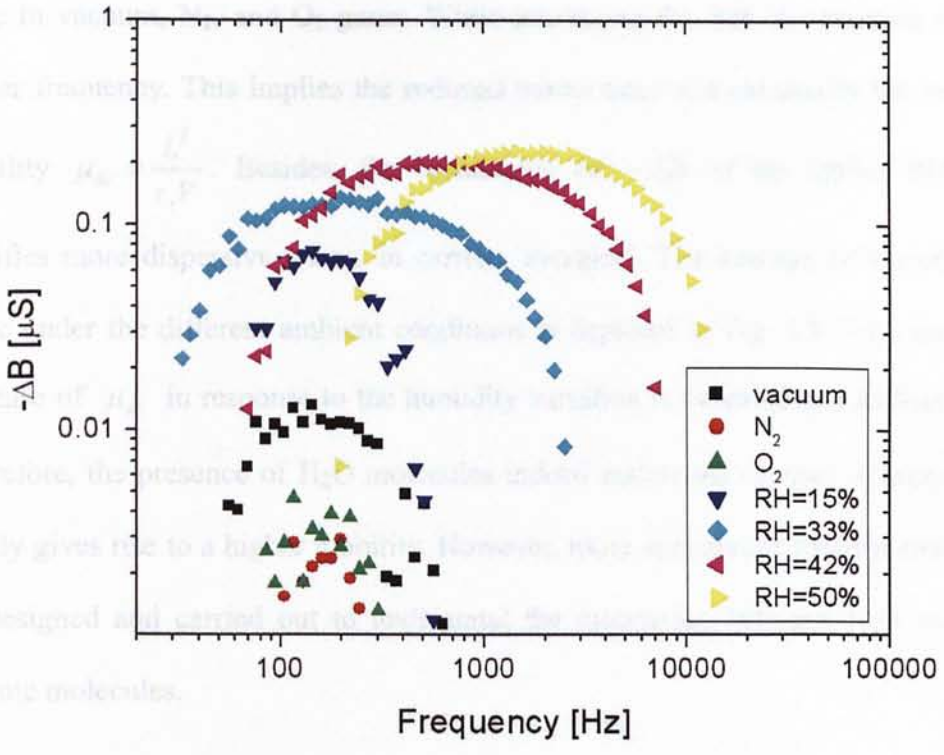

Figure 5.7. Double-logarithmic plot of the negative differential susceptance deduced from Fig. 5.6.

Fig. 5.6 shows the frequency dependent capacitance of Au/CuPc(500nm)/Au device as a function of frequency under the different ambient conditions at a dc bias of 2 V. At high frequency the capacitance is equal to the geometric capacitance $C_{geo} = \varepsilon_r \varepsilon_0 A / L$ (ε_0 is the vacuum permittivity, $\varepsilon_r \approx 2.78$ the relative dielectric constant of CuPc). Small inductive effect is found in a distinct frequency range, as discussed in Chapter 2, which is related to the carrier relaxation. This effect is more clearly visualized by plotting the negative differential suspectance $-\Delta B = -\omega(C - C_{geo})$ as a function of frequency. Fig. 5.7 displays $-\Delta B(\omega)$ at a dc bias of 2 V under the different ambient conditions. The relaxation time has a relation $\tau = 1/f \approx 2 \times \tau_t$, with τ_t be the transit time of carrier. Both can be derived from the

position of the $-\Delta B$ maximum. The maximum positions of $-\Delta B$ are almost the same in vacuum, N_2, and O_2 gases. While increasing the RH, the position shifts to higher frequency. This implies the reduced transit time and eventually the increased mobility $\mu_{dc} = \frac{L^2}{\tau_t V}$. Besides, the broadening of $-\Delta B$ at the higher RH levels signifies more dispersive nature in carriers transport. The average hole mobility of CuPc under the different ambient conditions is depicted in Fig. 5.8. An exponential increase of μ_{dc} in response to the humidity variation is obtained at a dc bias of 2 V. Therefore, the presence of H_2O molecules indeed assists the carriers in hopping and finally gives rise to a higher mobility. However, more appropriate experiments should be designed and carried out to understand the interaction between H_2O and CuPc organic molecules.

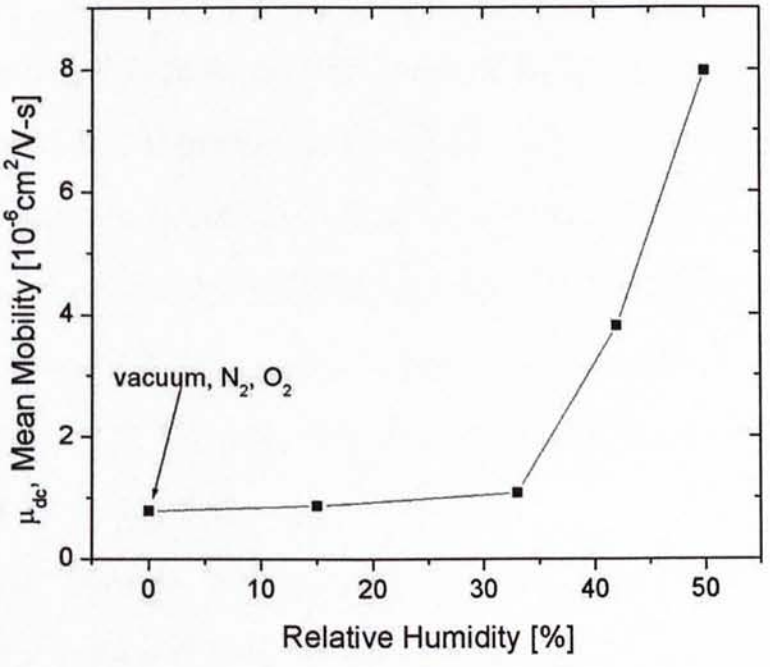

Figure 5.8. The average hole mobility μ_{dc} of 500 nm-thick CuPc thin film at a dc bias of 2 V under various conditions: vacuum, N_2 gas, O_2 gas, and air at different RH levels.

5.4 Conclusions

In summary, the static and dynamic behaviors of Au/CuPc/Au devices under different ambient conditions are demonstrated by *J-V* measurements and admittance spectroscopy, respectively. From the experimental results, it is found that there is no significant change in device performance in pure N_2 and O_2 gases. However, when the devices are exposed to air at different RH levels, the current magnitudes largely increase. By exploiting admittance spectroscopy, it is found the hole mobility increases and becomes more dispersive at the higher RH levels. Also this unequivocally that H_2O molecules assist the carrier in hopping.

Reference

[1] Z. T. Zhu, J. T. Mason, R. Dieckmann, and G. G. Malliaras, Appl. Phys. Lett. **81**, 4643 (2002).

[2] B. Crone, A. Dodabalapur, A. Gelperin, L. Torsi, H. E. Katz, A. J. Lovinger, and Z. Bao, Appl. Phys. Lett. **78**, 2229 (2001)

[3] L. Torsi, A. Dodabalapur, L. Sabbatini, and P. G. Zambonin, Sens. Actuators B **67**, 312 (2000)

[4] L. Torsi, A. Dodabalapur, N. Cioffi, L. Sabbatini, and P. G. Zambonin, Sens. Actuators B **77**, 7 (2001)

[5] M. Passard, A. Pauly, J. -P. Blanc, S. Dogo, J. -P. Germain and C. Maleysson Thin Solid Films **237**, (272) 1994.

[6] M. I. Newton, T. K. H. Starke, G. McHale and M. R. Willis, Thin Solid Films **360**, 10 (2000).

[7] M. I. Newton, T. K. H. Starke, M. R. Willis and G. McHale, Sensors and Actuators B: Chemical **67**, 307 (2000).

[8] Q. Zhou and R. D. Gould, Thin Solid Film **317**, 432 (1998).

[9] T. D. Anthopoulos, and T. S. Shafai, App. Phys. Lett. **82**, 1628 (2003).

[10] D. H. Dunlap, P. E. Parris, and V. M. Kenkre, Phys. Rev. Lett. **77**, 542 (1996).

[11] S. V. Novikov, D. H. Dunlap, V. M. Kenkre, P. E. Parris, and A. V. Vanikov, Phys. Rev. Lett. **81**, 4472 (1998).

[12] Y. Sakai, Y. Sadaoka, M. Matsuguchi, Sen. & Actu. B **35-36**, 85 (1996).

[13] E. V. Faassen and H. Kerp, Sen. & Actu. B **88**, 329 (2002).

Chapter 6

Summary and future work

Summary

In this thesis an investigation is systematically performed on various charge carrier transport properties of organic solid – copper phthalocyannie (CuPc) films under various trapping situations and ambient conditions.

By increasing the substrate temperature, crystalline nano spaghetti-like copper phthalocyannie (CuPc) is grown in the preferential directions, clearly indicating the propensity of CuPc to form crystallinities. However, the large number of grain boundaries, and the crossovers prevent the crystalline CuPc from fabricating functional devices, due to the numerous pin-holes. From the variable-temperature *J-V* measurements, the trap density $H_t = (5.42 \pm 0.34) \times 10^{16}\,\mathrm{cm}^{-3}$ and the characteristic trap energy $E_t = 0.14 \pm 0.1$ eV of CuPc are elicited in the trap filling region. The values are comparable with those found among other organic solids. The dynamics of holes is further interrogated by a unique characterization technique, i.e., admittance spectroscopy. In the case of the low bias region, the average mobility and field-dependent coefficient are deduced to be $(2 \pm 0.5) \times 10^{-7}$ $\mathrm{cm}^2/\mathrm{Vs}$ and $0.017 \pm 0.001\,(\mathrm{V/cm})^{-1/2}$, respectively. The measured data are in good agreement with those derived from a complementary study by dark current space-charge-limited

(DI-SCL) transient current measurements. The appearance of the conventional DI-SCL temporal profile unequivocally manifests the formation of the Ohmic contact at the Au/CuPc interfaces. In the high bias region, a large negative capacitance (i.e., equivalently, strong inductive effect) is found by admittance spectroscopy. By concurrently exploiting the current-voltage (*J-V*) and capacitance-voltage (*C-V*) characteristics of the Au/CuPc/Au devices, the negative capacitance is found to occur at the bias within the trap filling region. The slow trap filling process is deemed to be responsible for the distinct inductive effect. The study of carrier dynamics in CuPc is further extended under various ambient conditions. The influence of O_2 and N_2 gases is very small when compared with the humidity effect. A factor of a few times increase in the hole mobility is found, when the relative humidity (RH) reaches at a level of 50%. It is also noted that the hole mobility becomes more dispersive at higher RH levels. The deduced mobility under the various conditions clearly demonstrate that water molecules assist the hole carriers during hopping.

Future work

Although numerous pin holes are found in CuPc films prepared in high substrate temperature (>100°C), the interesting morphology maybe possible to increase the efficiency of organic solar cell by increasing the contact area between donor and acceptor materials. Recently, blend structure of polymer solar cell with interpenetrating network of the donor and acceptor materials has been proven that it can increase the exciton diffusion efficiency by 50%. By using the crystalline nano rod-like CuPc, a similar structure is possible to be fabricated. The problem of pin holes can be solved by evaporating a buffer layer of CuPc thin film on substrate (ITO), which is controlled at room temperature. In order to grow crystalline nano rod-like CuPc on the buffer layer, the substrate is increased to around 120°C during evaporation. Finally an acceptor material (e.g. C_{60}) and an anode (e.g Al) are evaporated on top of CuPc. Fig. 6.1 shows the illustrated structure of this idea.

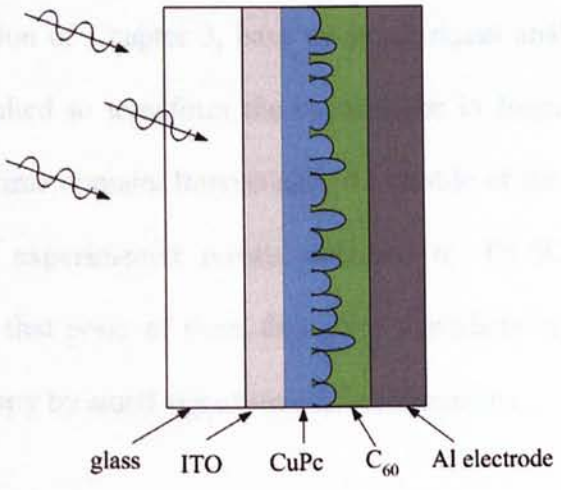

Figure 6.1. Illustrated structure to improve solar cell performance by inserting a layer of crystalline nano rod-like CuPc in between donor and acceptor materials.

In Chapter 3, the capability of using admittance spectroscopy to investigate the carrier relaxation processes in organic solid films is demonstrated. Although conventional time-of-flight (TOF) method can extract the mobility of carrier directly, admittance spectroscopy can quantitatively provide more information in different carrier relaxation processes (e.g. carrier mobility, trapping and dispersivity). Nevertheless, more experimental evidences in different material systems (e.g. doped or bilayer) and theoretical studies are desired to polish this characterization technique.

It has been shown that the behavior of dispersive carrier transport is thickness dependent, however, the nature of dispersive transport is still ambiguous. There are lots of debates on whether it is induced by positional disorder or energetic disorder of organic solid films. By carrying the admittance spectroscopy as a function of temperature, the energetic dependence of dispersive behavior can be explored. If the carrier transport more dispersive in lower temperature, the wide of the capacitance minimum will become broadened.

In the final section of Chapter 3, base on small signal analysis, inverse cosine transformation is applied to transform the capacitance in frequency domain to the relaxation current in time domain. Interestingly the profile of the relaxation current is very similar to the experimental results obtained by DI-SCL transient current measurements. From that point of view, this gives a predictable hint to evaluate the admittance spectroscopy by small signal time domain analysis.

Appendix A

Derivation of complex admittance for carrier transport in organic semiconductor

The complex admittance is derived by considering the time-dependent space-charge-limited current. Two basic equations which must be solved to obtain the time-dependence of the injection current are the total current density equation

$$J(t) = q\rho(x,t)\mu(t)E(x,t) + \varepsilon\frac{\partial E(x,t)}{\partial t} \tag{1}$$

and the Poisson equation

$$(\varepsilon/q)\frac{\partial E(x,t)}{\partial x} = \rho(x,t) \tag{2}$$

with $\rho(x,t)$ the time-dependent local hole density and ε the dielectric constant of the organic material. Moreover, in case of dispersive transport, the mobility μ is taken time dependent as well. At the metal/organic interface, an Ohmic injection contact is modeled by applying the boundary condition $E(0,t) = 0$.

In steady-state, the electric field is independent of time $\frac{\partial E(x,t)}{\partial t} = 0$. By combining Eqs. (1) and (2), the dc electric field and hole density become

$$E_{dc}(x) = \sqrt{\frac{2J}{\varepsilon\mu_{dc}}}x^{1/2} \tag{3}$$

$$\rho_{dc}(x) = \frac{\varepsilon}{2q}\sqrt{\frac{2J}{\varepsilon\mu_{dc}}}x^{-1/2} \tag{4}$$

In case of space-charge-limited current model, the current density – voltage

characteristics is described by the famous Mott-Gurny square law

$$J_{SCLC} = \frac{9}{8}\varepsilon\mu_{dc}\frac{V^2}{L^3} \tag{5}$$

where $\mu_{dc} = \frac{L^2}{\tau_t V}$. Therefore, from Eqs. (3) and (4), the dc electric field and hole density become

$$E_{dc}(x) = \frac{3\sqrt{L}}{2\tau_t\mu_{dc}}x^{1/2} \tag{6}$$

$$\rho_{dc}(x) = \frac{3\varepsilon\sqrt{L}}{4q\tau_t\mu_{dc}}x^{-1/2} \tag{7}$$

By separating the steady-state and time dependent contributions in Eqs. (1) and (2)

$$\begin{cases} E(x,t) = E_{dc}(x) + e(x,t) \\ \rho(x,t) = \rho_{dc}(x) + \vartheta(x,t) \\ J(t) = J_{dc} + j(x,t) \end{cases} \tag{8}$$

The resulting small time-dependent signal become

$$j(t) = q\mu(t)\rho_{dc}e(x,t) + \varepsilon\mu(t)E_{dc}\frac{\partial e(x,t)}{\partial x} + \varepsilon\frac{\partial e(x,t)}{\partial t} \tag{9}$$

The first term on the right-hand side of Eq.(9) describes the response of the dc charge density in the device. The second term gives the current due to the additional time-dependent injected charge-carrier density, the last term attributes to the displacement current by dipole relaxation. Since the admittance Y is equals to i_{ac}/v_{ac}, the ac electric field in Eq. (9) should be solved by considering the first order differential equation. Put $e(x,t) = e(x)e^{i\omega t}$ and apply Fourier transform, Eq. (9), giving

$$j(\omega) = q\mu(\omega)\rho_{dc}e(x) + \varepsilon\mu(\omega)E_{dc}\frac{\partial e(x)}{\partial x} + i\omega\varepsilon e(x) \tag{10}$$

The dc components in Eq.(10) can be eliminated by substituting Eqs. (3) and (4), giving

$$j(\omega)=\frac{3\varepsilon\sqrt{L\tilde{\mu}(\omega)}}{4\tau_t}x^{-1/2}e(x)+\frac{3\varepsilon\sqrt{L\tilde{\mu}(\omega)}}{2\tau_t}x^{1/2}\frac{\partial e(x)}{\partial x}+i\omega\varepsilon e(x) \quad (11)$$

with normalized mobility $\tilde{\mu}(\omega)=\mu(\omega)/\mu_{dc}$. By solving the above first order equation, $e(x)$ becomes

$$e(x)=\frac{j(\omega)}{i\omega\varepsilon}\left[1-\frac{3\sqrt{L\tilde{\mu}(\omega)}}{4i\omega\tau_t}x^{-1/2}\left(1-e^{\frac{-4i\omega\tau_t}{3\sqrt{L\tilde{\mu}(\omega)}}x^{1/2}}\right)\right] \quad (12)$$

Since $v_{ac}=\int_0^L e(x)dx$, therefore

$$v_{ac}=\frac{j(\omega)}{i\omega\varepsilon}\left[L-\frac{3L\tilde{\mu}(\omega)}{2i\omega\tau_t}-2L\left(\frac{3\tilde{\mu}(\omega)}{4\omega\tau_t}\right)^2\left(1-e^{\frac{-4i\omega\tau_t}{3\tilde{\mu}(\omega)}}\right)\right] \quad (13)$$

Substitute the normalized frequency $\Omega=\omega\tau$ into Eq. (13), giving

$$v_{ac}=\frac{j(\Omega)\tau_t L}{\Omega^3\varepsilon}\left[-i\Omega^2+1.5\tilde{\mu}(\Omega)\Omega+2i\left(0.75\tilde{\mu}(\Omega)\right)^2\left(1-e^{-i4\Omega/3\tilde{\mu}(\Omega)}\right)\right] \quad (14)$$

As $Y(\Omega)=i_{ac}/v_{ac}$, where $i_{ac}=Aj_{ac}$ and A is the active area of the device, as a result

$$Y(\Omega)=\frac{\varepsilon A}{L\tau_t}\frac{\Omega^3}{2i\left(0.75\tilde{\mu}(\Omega)\right)^2\left(1-e^{-i4\Omega/3\tilde{\mu}(\Omega)}\right)+1.5\tilde{\mu}(\Omega)\Omega-i\Omega^2} \quad (15)$$

Eq.(15) describes the frequency-dependent electrical response of the carriers inside the organic solid film. This provides a concrete explanation on the experimental results of the carrier transport behavior obtained by admittance spectroscopy.

Appendix B

Derivation of transient relaxation current by Fourier analysis of frequency-dependent capacitance

The capacitance of a two-terminal semiconductor device is defined as

$$C(\omega) = \frac{1}{\omega}\mathrm{Im}[Y(\omega)] \tag{1}$$

where the admittance $Y(\omega)$ is

$$Y(\omega) = \frac{\delta I(\omega)}{\delta V(\omega)} \tag{2}$$

The method based on the Fourier analysis involves calculation of the transient response of the device to a small time-dependent voltage excitation (usually in the form of a step-function) applied at the time $t = 0$. Admittance is calculated as the ratio of the Fourier components of the transient current $\delta I(t) = I(t) - I(0^-)$ and voltage $\delta V(t) = V(t) - V(0^-)$. This method will be used to relate the properties of capacitance-frequency (*C-F*) characteristics to the time-domain behavior of the transient current as shown below.

By considering the transient current in a semiconductor device in response to a applied voltage step ΔV:

$$\delta V(t) = V(t) - V(0^-) = \Delta V \theta(t) \tag{3}$$

$$\begin{aligned}\delta I(t) &= I(t) - I(0^-) \\ &= \left[I(t) - I(\infty)\right]\theta(t) + \left[I(\infty) - I(0^-)\right]\theta(t)\end{aligned} \tag{4}$$

where $\theta(t)$ is the unity step function. The quantities with "-" superscript denotes single-sided value of the discontinuous functions, for example, $V(0^-) = \lim_{\tau \to 0} V(\tau)$, $\tau < 0$. In (4), the transient current $\delta I(t)$ is decomposed into the step-like component $[I(t) - I(\infty)]\theta(t)$ (DC conductivity) and transient current $\delta J(t) = [I(t) - I(\infty)]\theta(t)$, so that $\delta J(t) \to 0$ as $t \to \infty$. Substituting the Fourier expansions of (3) and (4) into Eq. (2), and noting that $\int_{-\infty}^{\infty} \theta(t) e^{-i\omega t} dt = 1/(i\omega)$, we obtain the following expression for admittance:

$$Y(\omega) = \frac{i\omega}{\Delta V} \int_0^{\infty} \delta I(t) e^{-i\omega t} dt \tag{5}$$

Separating the real and imaginary parts in Eq.(5), we obtain the expressions for the capacitance as follows:

$$C(\omega) = \frac{1}{\Delta V} \int_0^{\infty} \delta J(t) \cos \omega t \, dt \tag{6}$$

Generally, the transient current $\delta J(t)$ contains an impulse-like component and a slowly varying relaxation component:

$$\delta J(t) = C_{geo} \Delta V \delta(t) + \delta j(t) \tag{7}$$

Here, $\delta(t)$ is the delta-function. The impulse-like component corresponds to a current charging the geometric capacitance C_{geo}. Physically, this current is due to the displacement current in the semiconductor. The relaxation component $\delta j(t)$ can be due to the charge carrier transport, trapping, impact ionization, and other physical processes. Substituting Eq.(7) into (6), the relation between frequency-dependent

capacitance $C(\omega)$ and relaxation current $\delta j(t)$ is obtained:

$$C(\omega) = C_{geo} + \frac{1}{\Delta V}\int_0^{\infty} \delta j(t)\cos(\omega t)\,dt \tag{8}$$

By applying the inverse cosine transform on Eq.(8), we obtain the expression of relaxation current in terms of frequency-dependent capacitance as follows:

$$\delta j(t) = \frac{2\Delta V}{\pi}\int_0^{\infty} \left[C(\omega) - C_{geo}\right]\cos\omega t\,d\omega \tag{9}$$

Eqs.(8) and (9) provide very useful information to interpret the frequency-dependent and time-dependent charge relaxation processes in many semiconductor devices.

Appendix C

Simulation program for admittance spectroscopy

```
%%%
```

```
    if m == 1
        Vdc = 0.0001;                    % applied voltage (V)
    elseif  m == 2;
        Vdc =2;                          % applied voltage (V)
    elseif  m == 3;
        Vdc = 4;                         % applied voltage (V)
    elseif  m == 4;
        Vdc = 8;                         % applied voltage (V)
    end
    Edc = Vdc/L;                         % applied electric field (V/cm)
%%%%%%%%% distribution of transit time %%%%%%%%%
for k = 1:5
    W = 2;              % inverse wide of transit time distribution
    if k == 1
        tor_t = exp((k-3)/W)*L/(udc*Edc);
    elseif  k == 2;
        tor_t = exp((k-3)/W)*L/(udc*Edc);

    elseif  k == 3;
        tor_t = exp((k-3)/W)*L/(udc*Edc);

    elseif  k == 4;
        tor_t = exp((k-3)/W)*L/(udc*Edc);

    elseif  k == 5;
        tor_t = exp((k-3)/W)*L/(udc*Edc);

    end

init_freq = 10^6;                    % initial frequency (Hz)
freq = init_freq;
admit(1:500)=0;                      % data range
for j = 1:500

if freq > 10                         % upper bound is 2MHz
    freq_temp(j) = freq;
    nor_omg = 2*pi*freq*tor_t;       % normalized frequency
```

```
%%%%%%%%% Despersive Mobility %%%%%%%%%
u = (1 + M*(i*nor_omg)^(1-alpha))*3/4;

%%%%%%%%%%%%%% Calculation of admittance %%%%%%%%%%%%%%%
admit(j) =
(abs_els*rev_els/tor_t)*(A/L)*(nor_omg^3)/(2*i*(u^2)*(1-exp(-i*nor_omg/u))+2*u*
nor_omg-i*nor_omg^2);          % admittance equation

freq = 0.9 * freq;                          % 10% decrement of frequency
tempG(k,j) = abs(admit(j));                 % conductance
tempC(k,j) = imag(admit(j))/(2*pi*freq_temp(j));      % capacitance
tempNegDelB(k,j) = -2*pi*freq_temp(j)*(tempC(k,j) - tempC(k,1));      % negative
differential suspentance

    end
end
end

%%%%%%%% sum up dispersive effect for different transit times %%%%%%%%
G(m,:)=(tempG(1,:)+tempG(2,:)+tempC(3,:)+tempG(4,:)+tempG(5,:))/5;
C(m,:)=(tempC(1,:)+tempC(2,:)+tempC(3,:)+tempC(4,:)+tempC(5,:))/5;
negDelB(m,:)=
(tempNegDelB(1,:)+tempNegDelB(2,:)+tempNegDelB(3,:)+tempNegDelB(4,:)+temp
NegDelB(5,:))/5;
end

%%%%%%%%%% plot conductance %%%%%%%%%%%%%
figure;
for k=1:num_curve
    if k == 1
        loglog(freq_temp(:),G(k,:), 'k-'); hold on;
    elseif  k == 2;
        loglog(freq_temp(:),G(k,:), 'r-'); hold on;
    elseif  k == 3;
        loglog(freq_temp(:),G(k,:), 'g-'); hold on;
     elseif  k == 4;
        loglog(freq_temp(:),G(k,:), 'b-'); hold on;
```

```
            elseif   k == 5;
        loglog(freq_temp(:),G(k,:), 'c-'); hold on;
    end
end
title('Conductance v.s Frequency');
xlabel('Frequency [Hz]');
ylabel('Conductance [S]');
legend('V_b_i_a_s = 0V','V_b_i_a_s = 0.5V','V_b_i_a_s = 1V','V_b_i_a_s = 1.5V',4);

%%%%%%%%%%% plot capacitance %%%%%%%%%%%%%
figure;
for k=1:num_curve
    if k == 1
        semilogx(freq_temp(:),C(k,:)/1e-9, 'k-'); hold on
    elseif   k == 2;
        semilogx(freq_temp(:),C(k,:)/1e-9, 'r-'); hold on;
    elseif   k == 3;
        semilogx(freq_temp(:),C(k,:)/1e-9, 'g-'); hold on;
            elseif   k == 4;
        semilogx(freq_temp(:),C(k,:)/1e-9, 'b-'); hold on;
            elseif   k == 5;
        semilogx(freq_temp(:),C(k,:)/1e-9, 'c-'); hold on;
    end
end
title('Capacitance v.s Frequency');
xlabel('Frequency [Hz]');
ylabel('Capacitance [nF]');
legend('V_b_i_a_s = 0V','V_b_i_a_s = 1V','V_b_i_a_s = 2V','V_b_i_a_s = 3V',1);

%%%%%%%%%% plot negative differential suspectance %%%%%%%%%%
figure;
for k=1:num_curve
    if k == 1
        loglog(freq_temp(:),negDelB(k,:), 'k-'); hold on
    elseif   k == 2;
        loglog(freq_temp(:),negDelB(k,:), 'r-'); hold on;
    elseif   k == 3;
        loglog(freq_temp(:),negDelB(k,:), 'g-'); hold on;
```

```
            elseif   k == 4;
        loglog(freq_temp(:),negDelB(k,:), 'b-'); hold on;
            elseif   k == 5;
        loglog(freq_temp(:),negDelB(k,:), 'c-'); hold on;
    end
end
title('Negative differential suspectance v.s Frequency');
xlabel('Frequency [Hz]');
ylabel('-      B [S]');
legend('V_b_i_a_s = 0V','V_b_i_a_s = 1V','V_b_i_a_s = 2V','V_b_i_a_s = 3V',1);
```

%%%%%%%%%%%%% end of program %%%%%%%%%%%%%%

Appendix D

Publications which contributed to this thesis

Journal:

1. S. W. Tsang, J. B. Xu, W. M. Lau, and H. L. Kwok, "*Dynamics of hole transport and negative capacitance in copper phthalocyanine (CuPc)*", (**Submitted to APL**).

Conference:

2. S. W. Tsang, J. B. Xu, M. S. Xu, and Harry H. L. Kwok, "*Negative Capacitance in Au/Copper Phthalocyanine (CuPc)/Au Investigated by Impedance Spectroscopy*", Material Research Society, MRS 2003 Fall Meeting Symposium J: Interfaces in Organic and Molecular Electronics (**CONTROL ID: 48290**).
3. S. W. Tsang and J. B. Xu, A. Jan, "*Trap Filling Induced Negative Capacitance in Au/CuPc/Au*" 6th International Symposium on Functional π-electron System, Cornell University, Ithaca, New York. (**BP.1.0**)
4. S. W. Tsang, J. B. Xu, and A. Jan, "*Dispersive Holes Transport In Copper Phthalocyanine (CuPc) Under Various Ambient Conditions*", 6th International Symposium on Functional π-electron System, Cornell University, Ithaca, New York. (**DP.49**)